Aeroacoustic Installation Effects on a Propeller-Driven Strut-Braced Wing Aircraft

Aeroacoustic Installation Effects on a Propeller-Driven Strut-Braced Wing Aircraft

Emanuele Sticchi* and Daniele Ragni† and Damiano Casalino‡
Delft University of Technology, Flow Physics and Technology Department, Kluyverweg 1, 2629 HS Delft, Netherlands

Francesco Avallone§
Polytechnic University of Turin, Department of Mechanical and Aerospace Engineering, Corso Duca degli Abruzzi 24, Torino, 10129, Italy

The Strut-Braced Wing (SBW) is a promising design for reducing aircraft emissions. However, the integration with propellers introduces complex aerodynamic and aeroacoustic interactions. This study investigates the aerodynamic installation effects of a propeller-driven SBW aircraft in high-lift conditions. High-fidelity numerical simulations are carried out using a very-large eddy simulation approach coupled with a lattice Boltzmann solver. Two propeller rotation configurations are analyzed: clockwise and counter-clockwise. The aeroacoustic analysis is conducted using a hybrid CFD/CAA approach based on the Ffowcs-Williams and Hawkings analogy. The propeller slipstream alters the wing loading, reducing aerodynamic efficiency by approximately 7–8% compared to the propeller-off configuration. New insights are provided into the role of the nacelle in modifying the wing loading. Aerodynamic efficiency benefits are found on the strut, experiencing a 21–25% lift increase with minimal drag impact caused by the slipstream. The blade loading exhibits an asymmetry due to wing-induced upwash, amplifying tonal noise components at harmonics of the blade passing frequency. The effects of propeller wake impingement on both the wing and strut are analyzed, highlighting distinct interaction mechanisms and their implications on unsteady surface pressure. The noise footprint at certification locations for the outboard up configuration is 4 EPNdB lower than the inboard up case. The reason is that when the blade moves downward on the inboard side, the fuselage blocks the sound waves from the propeller blades, creating a shadow region beneath the aircraft. These findings highlight the importance of component positioning in aircraft design to

A preliminary version of this work was presented as Paper AIAA 2024-3012 at the 30th AIAA/CEAS Aeroacoustics Conference, Rome, Italy, 4–7 June 2024.

*PhD Candidate, Delft University of Technology, Faculty of Aerospace Engineering, Department of Flow Physics and Technology, Wind Energy Section, Aeroacoustics group, Corresponding author. Email: e.sticchi@tudelft.nl

†Associate Professor, Delft University of Technology, Faculty of Aerospace Engineering, Department of Flow Physics and Technology, Wind Energy Section, Aeroacoustics group, d.ragni@tudelft.nl, AIAA Member

‡Full Professor, Delft University of Technology, Faculty of Aerospace Engineering, Department of Flow Physics and Technology, Wind Energy Section, Aeroacoustics group, d.casalino@tudelft.nl

§Full Professor, Polytechnic University of Turin, Department of Mechanical and Aerospace Engineering, francesco.avallone@polito.it, AIAA Member

reduce far-field noise emissions.

I. Nomenclature

a_∞	=	Freestream speed of sound
BPF	=	Blade passing frequency
C_T	=	Thrust coefficient
C_L	=	Lift coefficient
C_D	=	Drag coefficient
C_Q	=	Torque coefficient
D	=	Propeller diameter
$EPNL$	=	Effective perceived noise level
f	=	Frequency
h	=	Flight altitude
L_p	=	Sound pressure level
ℓ	=	Fuselage length
M_∞	=	Freestream Mach number
$OSPL$	=	Overall sound pressure level
$PNLT$	=	Perceived noise level with tone correction
p	=	Fluid pressure
q_∞	=	Freestream dynamic pressure
Re_∞	=	Freestream Reynolds number
R	=	Propeller radius
RoC	=	Rate of climb
RPM	=	Revolutions per minute
r	=	Blade radial coordinate
T	=	Rotor revolution period
t	=	Time
V	=	Fluid velocity
x, y, z	=	Components of the spatial coordinate vector
$\mathbf{x}$	=	Spatial coordinate vector
α	=	Angle of attack
γ_l	=	Non-dimensional Lift distribution

γ_d = Non-dimensional Drag distribution

Δt = Time step

ϵ = Turbulent dissipation rate

κ = Turbulent kinetic energy

ρ = Fluid density

τ = Relaxation time

τ_{eff} = Effective relaxation time

ω = Vorticity magnitude

ω_y = y-component of vorticity vector

Subscripts

∞ = Freestream

II. Introduction

The need to decarbonise aviation is driving the industry to explore new technologies for innovative aircraft design that offer significant potential for reducing drag and weight and that employ electric/hydrogen-based propulsion systems. Among the explored configurations, the strut-braced wing is one of the most promising for short-range entry into service. This configuration leverages reduced induced drag by increasing the wing span and addresses the structural challenges of ultra-high aspect ratio wings by adding a streamlined element, i.e., the strut, which connects the wing to the fuselage, alleviating the wing bending loads. Several studies have highlighted the advantages of the strut-braced wing configuration at the aircraft level [1–6]. In particular, methods for efficient aerodynamic design have been developed, showing significant performance improvements for transonic flight [7, 8]. Numerous research projects have also explored the potential benefits of this configuration for transonic aviation [6, 9, 10]. Simultaneously, the Clean Aviation HERWINGT project focuses on adapting this design to hybrid-electric regional transport.

In the design process of a propeller-driven strut-braced wing configuration, it is crucial to consider installation effects, which refer to changes in performance, noise, and structural behavior when a propeller is integrated into the aircraft system. These effects arise from the interaction between the propeller and other components, such as the wing and fuselage, as well as the influence of the surrounding flow field. A key installation effect is the aerodynamic interaction between the propeller slipstream and the wing, which can significantly impact lift, drag, and overall aerodynamic performance [11–14]. Additionally, acoustic interactions occur when propeller-generated sound waves interact with the fuselage, potentially altering noise levels and vibration characteristics [15, 16].

In this framework, propeller-wing interaction effects can be analyzed by considering three key factors: how the propeller influences wing loading, how the wing affects blade loading, and the unsteady pressure fluctuations caused by

the propeller's wake on the downstream body. The propeller affects the wing loading due to two main effects. The first is the increase in axial velocity caused by the propeller slipstream, which locally increases the lift produced by the wing. The second effect is the swirl velocity caused by the rotating blades. This swirl component modifies the direction of the incoming flow and changes the effective angle of attack on the wing. Specifically, when the propeller blade moves from the wing's pressure side to the suction side, it increases the effective angle of attack on the wing section in its wake. Conversely, when the blade moves from the suction side to the pressure side, it decreases the effective angle of attack [14]. On the other hand, the wing's influence on blade loading is primarily driven by the upwash caused by wing-bound vorticity. This wing-induced velocity alters the angle of attack experienced by the blade elements, causing a decrease when the blade moves from the suction to the pressure side of the wing and an increase when moving from the pressure to the suction side, similar to the effect of a non-zero inflow angle. Additionally, as the vortices shed by the propeller blades reach the wing, they interact with the boundary layer, leading to increased wall shear stress, turbulence, and pressure fluctuations [17, 18]. A first analysis of the system has been carried out in the literature with simplified models, such as the vortex-body orthogonal and streamwise interference [19, 20]. This simplified model studies the interaction between a cylindrical vortex and a downstream airfoil. The vortex can be oriented either orthogonal or parallel to the freestream direction. The parameters governing the interaction are identified in:

- **Impact parameter**: relative magnitude of the impact velocity (i.e., the velocity of the body relative to the vortex) to swirl velocity.
- **Axial flow parameter**: the relative magnitude of the axial core velocity and the swirl velocity.
- **Thickness parameter**: the relative thickness of the body with respect to the vortex core radius.

The parameters mentioned above fully determine the intensity of the interaction and the relative importance between potential and viscous effects. In the case of a vortex perpendicular to the freestream, two distinct interaction regimes can be distinguished. In the strong vortex regime, occurring at high swirling velocity and low impact parameter, the vortex strongly interacts with the wing's boundary layer before impingement, causing rapid ejection of boundary layer vorticity [21, 22]. In the weak vortex regime, which occurs at high impact parameter and low thickness parameter, the vortex impinges without boundary layer separation, with weaker interaction before impingement [23, 24]. The axial flow within the vortex creates asymmetry, resembling a piston in a tube, and influences the vortex core radius, as confirmed by experimental studies [25, 26].

Despite the knowledge acquired on the fundamental aerodynamic mechanisms of vortex-body interaction, a full-scale propeller wake-wing interaction is characterized by more complex phenomena. Multiple helical structures impinging on a lifting wing appear. Therefore, the interaction of the blade-tip vorticity with the boundary layer and the pressure gradient forming on the wing might lead to different scenarios, depending on the aircraft's cruise speed and the wing's loading. Recently, several studies have been conducted, with both numerical [17, 27, 28] and experimental [29, 30] methods on more realistic configurations. Muscari et al. [27] analyzed the wake interaction between a moderately

loaded one-blade marine propeller and a non-lifting wing using Detached Eddy Simulations. Visualizations of λ_2 and pressure spectra on the wing surface were employed to relate the unsteady loading on the wing to the tip and hub vortex dynamics. They found that the fluctuating pressure field caused by the tip vortex-wing interaction has a tonal contribution at the blade passing frequency (BPF) harmonics, with an intensity that suddenly drops moving to the aft portion of the wing. Distinct effects between wing pressure and suction side were observed and related to the different stretching mechanisms of the vortical flow on the two sides. Wang et al. [18] analyzed the characteristics of the wake dynamics of a propeller operating before a rudder, varying the angle of attack of the wing and the loading of the propeller. An increased complexity of the wake dynamics was shown at higher propeller loads and wing incidence. In contrast with the previous studies, which analyzed the propeller-body interaction only from a qualitative point of view, Posa et al. [17] presented a more quantitative analysis performed through WRLES. Their results were in agreement with the PIV measurement of Felli & Falchi [29], and an increased level of turbulent kinetic energy at the wing leading edge for lower advance ratios was reported. More recently, Felli [30] showed, in a study about the mechanisms of interaction between the wake of a marine propeller and a downstream non-lifting wing at high thickness parameters, that the interaction phenomenon was not affected by the propeller loading and the number of blades, as long as they are such that they do not induce wake destabilisation.

Although several research efforts have been conducted to shed light on these interactions, to the author's knowledge, no studies have examined propeller installation effects on a full-scale strut-braced wing aircraft. In particular, this study aims to investigate how the previously described interaction mechanisms are modified by the presence of a multi-component wing for two propeller rotating configurations: clockwise and anti-clockwise. The analysis focuses on the aerodynamic and acoustic installation effects arising from the propeller–wing interaction, while the comparison with a cantilever layout serves to isolate and quantify the specific contribution of the strut. Additionally, it will explore which wake interaction mechanisms impact the strut and how these interactions compare to those observed on the main wing. To this purpose, high-fidelity simulations are performed with a Very Large Eddy Simulation (VLES) approach applied to a Lattice Boltzmann Method (LBM) solver, and the acoustic effects in the far field are evaluated with a Ffowcs-Williams and Hawkings (FW-H) acoustic analogy.

The manuscript is structured as follows: the numerical methodology is described in Section III. The numerical setup and the analyzed geometry are presented in Section IV. The results are reported in Section V and are organized as follows: installation effects on the aircraft aerodynamic efficiency in Section V.A, on the wing and strut loadings in Section V.B, on the blade loadings in Section V.C, on the propeller wake dynamics and the consequent fluctuating pressure induced on the wing and strut in Section V.D and V.E, and on the aircraft far-field noise emission in Section V.F. Finally, the conclusions are summarized in Section VI.

III. Methodology

A. Flow Solver

The flow field was computed using the commercial flow solver PowerFLOW®, version 6-2022-R3, from Dassault Systèmes, which implements the LBM. The software has been extensively used to accurately predict noise generated in complex flow problems, specifically for full-vehicle configurations [31–39] and propulsive units [40–43].

In the LBM, the motion of a collection of fluid particles at the mesoscopic level is described using distribution functions. The Boltzmann transport equation, Eq. 1, is used to model the advection and collisions of fluid particles:

$$\frac{\partial f}{\partial t} + \mathbf{V} \cdot \boldsymbol{\nabla} f = C, \tag{1}$$

where $f(\mathbf{x}, t, \mathbf{V})$ is the probability density function representing the probability of finding, in the elementary volume $d\mathbf{x}$ around a spatial coordinate $\mathbf{x}$ and in the infinitesimal time interval $(t, t + \Delta t)$, a number of fluid particles with velocity in the interval $(\mathbf{V}, \mathbf{V} + d\mathbf{V})$. C is the collision operator, which accounts for particle velocity distribution changes due to momentum exchanges during collisions. Thus, the left-hand side of Eq. (1) describes the particle advection, whereas the right-hand side describes the collision process. Eq. (1) is discretised using a Cartesian grid (i.e., lattice) as follows:

$$f_i\left(\mathbf{x} + \mathbf{V_i}\Delta t, t + \Delta t\right) - f_i\left(\mathbf{x}, t\right) = C_i\left(\mathbf{x}, t\right)\Delta t, \tag{2}$$

where f_i, V_i, and C_i are the particle distribution function, the discrete particle velocity, and the collision operator along the i^{th} lattice direction.

In the current study, the velocity space is discretised into 19 discrete directions (D3Q19 model). A non-isothermal LB model is used in PowerFLOW®. This non-isothermal version solves an additional scalar transport equation for the total energy, ensuring energy conservation [44], and employs a regularized collision operator that removes spurious non-equilibrium moments to prevent numerical instabilities at high Mach numbers [45]. This model extends the capability of the D3Q19 scheme in the high-subsonic and transonic regimes, as relevant to the present study.

After solving Eq. (2), the macroscopic flow quantities can be obtained as follows:

$$\rho\left(\mathbf{x}, t\right) = \sum_i f_i\left(\mathbf{x}, t\right), \quad \rho\mathbf{u}\left(\mathbf{x}, t\right) = \sum_i \mathbf{V_i} f_i\left(\mathbf{x}, t\right). \tag{3}$$

For high-Reynolds-number flows, the turbulence modeling is incorporated into Eq. (2) by replacing the relaxation time, τ, in the collision operator [45] with an effective turbulent relaxation time:

$$\tau_{eff} = \tau + C_\mu \frac{\kappa^2/\epsilon}{\left(1 + \eta^2\right)^{1/2}}, \tag{4}$$

where $C_\mu = 0.09$ and η is a combination of local strain $\kappa|\mathbf{S}/\epsilon|$, local vorticity $\kappa|\omega/\epsilon|$ and local helicity parameters. The turbulent kinetic energy and the turbulent dissipation rate are obtained by solving a variant of the RNG κ-ϵ model [46]. Although the relaxation time is computed using a two-equation transport model, it is not used to compute an equivalent eddy viscosity or Reynolds stresses, such as in Reynolds-Averaged Navier-Stokes (RANS) models, but instead to re-calibrate the Boltzmann model to the characteristic time scales of a turbulent flow motion [47, 48]. This constitutes the essence of the LBM-VLES approach. Furthermore, to reduce the computational cost deriving from the use of a uniform Cartesian grid near solid walls, a pressure-gradient extended wall model is used to approximate the no-slip boundary condition [49].

B. Far-Field Acoustics Computation

Although the flow solver used is intrinsically suited for aeroacoustic calculations due to its low-dispersion and low-dissipation properties [50], the grid size required up to the microphone location makes a direct computation of far-field noise unfeasible. Therefore, this study employs a hybrid CFD/CAA approach. Specifically, far-field noise was computed using the tool *Opty∂B*-FWHFREQ®, which implements the permeable surface formulation of the FW-H acoustic analogy [51]. This formulation is the extension to three-dimensional flow fields of the frequency domain formulation proposed by Lockard [52]. The approach is consistent with an equivalent time-domain approach, but Fourier transforms are realised on the FW-H source terms before their propagation [53].

Since CFD simulations were performed employing a symmetry plane, the FW-H permeable surface was mirrored before the noise computation.

Sound spectra are computed by means of the Welch algorithm [54] using the Hanning function on windows of bandwidth ≈ 7 Hz and an overlapping coefficient around 0.5.

C. EPNL computation

The computational procedure implemented in the software *Opty∂B*-FOOTPRINT® was used to compute the Effective Perceived Noise Level (EPNL) on the ground following the FAR Part 36 procedure [55].

The approach relies on the permeable FW-H formulation to generate far-field noise signals on microphones distributed over a hemisphere centred on the aircraft reference frame. These are then used to obtain the hemisphere's Narrow-Band Noise (NBN) spectra. For each ground microphone and every 0.5-second flight sub-segment, the aircraft emission position is determined in the inertial reference frame. A ray-tracing method is applied to interpolate NBN spectra at the intersection points between the ray and the hemisphere, accounting for direct and reflected noise contributions. The interpolated spectra are then propagated to the ground, considering spherical spreading, atmospheric absorption, Doppler effects, amplitude correction, and ground reflection. Further mathematical details on the EPNL tool and its validation can be found in Casalino et al. [56].

This study used a hemisphere of $60m$ radius, discretised in 625 virtual microphones, as the sound source. Since CFD simulations were performed employing a symmetry plane, the noise hemisphere was mirrored before the projection of the spectra on the ground microphone carpet. The two contributions of the mirrored hemispheres are then added incoherently.

IV. Numerical setup

A. Aircraft Geometry

The aircraft geometry is depicted in Fig. 1. It consists of the strut-braced wing developed in the initial phase of the Clean Aviation project HERWINGT and the fuselage designed in the parent project HERA. The wing is the result of an aerodynamic optimization performed through the *in-house* optimization framework *WiMOT* described in Appendix .A to minimize aerodynamic drag in cruise condition, defined by $M_\infty = 0.5$, $Re = 5.5 \cdot 10^6$ 1/m, $C_L = 0.64$. During the optimization, six Bernstein coefficients were used for each side of the airfoils. The Bernstein coefficients were bounded between -1 and 1, a range chosen to ensure that the baseline airfoils provided by the HERWINGT partners were included within the design space. The wing airfoil geometries were constrained to have the same maximum thickness and internal area as the baseline ones. The variation in the twist angles was limited to $\pm 5°$. The chord length of the strut's airfoils and the longitudinal positions of the strut were constrained to have the root airfoil between 2 specified fuselage frames, whereas the tip airfoil of the strut was set between the wing spars. The design space of the span-wise position of the wing-strut attachment was restricted to two values: 60% or 66% of the wing span, according to preliminary aeroelastic studies. With a total of 136 design variables and a population size set to 200 chromosomes, the optimization cost was lower than 1000 CPU hours on 20 cores on an Intel(R) Xeon(R) CPU E5-2670v2 2.5 GHz.

In this design phase, the strut-wing junction was approximated with a vertical connection of height h_s between the strut tip and the wing. After analyzing the optimization results for different h_s values, the height of this connection was set to 30 cm. Following the results obtained by Tétrault [57], the strut junction was designed as an arched-shaped junction intersecting perpendicularly to the wing's lower surface. Furthermore, the strut root was installed to have a perpendicular intersection with the fuselage sponson. The fuselage was designed in the HERA project, assuming a regional transport aircraft with a maximum capacity of about 100 seats and a range of 500 km to 1000 km. In addition, since propeller and nacelle geometries were not available at the stage of the project when the analyses were conducted, the authors adopted characteristics based on information provided in the preliminary design phase. These include the propeller diameter, thrust, RPM, span-wise position, and the expected ratio between the propeller disk and nacelle diameter. Relevant data regarding the geometry can be found in Table 1, while the radial distributions of twist and chord length for one propeller blade are illustrated in Fig. 2. Seven aircraft configurations were examined to analyze the effects of different aircraft components. Specifically, three configurations were considered for each propeller rotation direction:

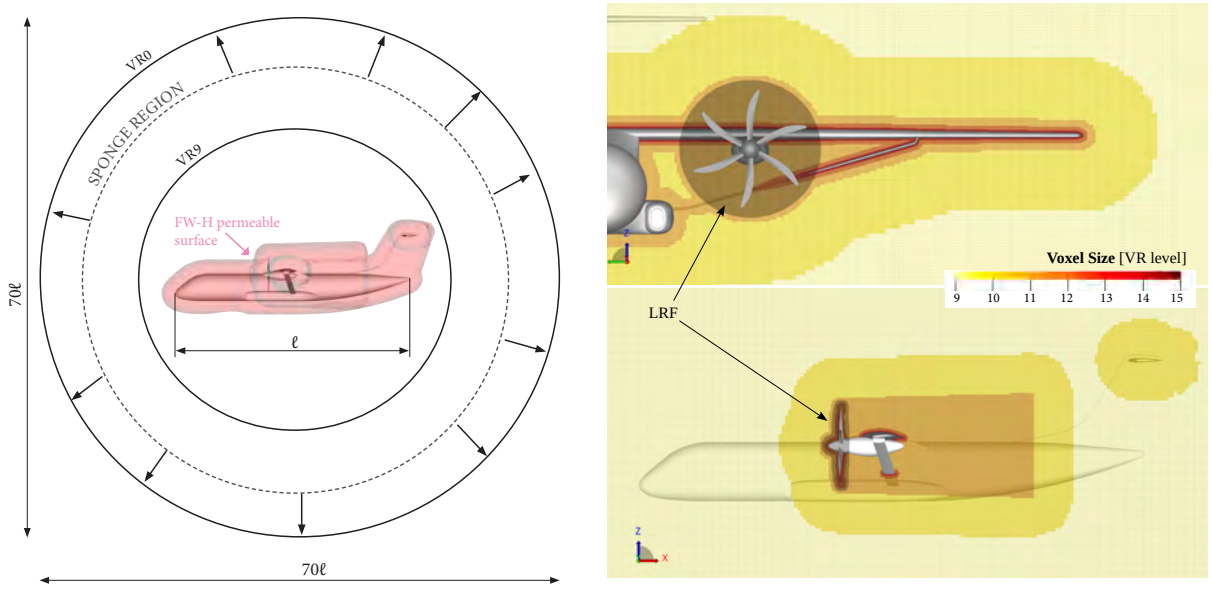

(a) (b)

Fig. 1 (a) Representation of the aircraft geometry and sketch of the computational domain. The domain boundaries and the resolution regions (VRs) are not drawn to scale. (b) Representation of the finer VR regions.

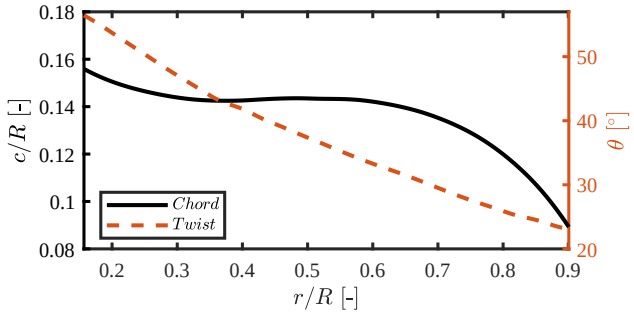

Fig. 2 Chord and twist angle radial distribution of the propeller blades.

the strut-braced wing aircraft with the engine installed, the cantilever version (same wing without the strut) with the engine installed, and the isolated engine. A propeller-off configuration, consisting of the aircraft geometry without the engine, was also included. Throughout the discussion, the configuration in which the propeller blades move upward on the inboard side will be referred to as "inboard up" (IU), while the configuration where the blades move upward on the outboard side will be called "outboard up" (OU). When not specified, the term "installed" always refers to the SBW installed configuration. Moreover, the authors will refer to the wing's upward side as the side where the propeller blades move from the wing pressure side to the wing suction side, and the wing's downward side as the side where the blades move from the suction side to the pressure side.

Table 1 Summary of geometrical parameters.

Description	Symbol	Value
Wing semi-span	b	17.62 m
Wing aspect ratio	AR	17
Mean aerodynamic chord	c_{mac}	2.134 m
Fuselage length	ℓ	30.75 m
Fuselage diameter	D_{fus}	3.45 m
Propeller diameter	D	5.02 m
Propeller RPM	RPM	1103 rpm
Number of blades	B	6

B. Flight condition and solver settings

The simulations were performed at high-lift low-speed conditions defined by $M_\infty = 0.20$, $h = 0$ m, $Re_\infty/c = 4.6 \cdot 10^6$ 1/m, $AoA = 10°$. These conditions were chosen according to the flight envelope defined for the SBW aircraft developed in the HERWINGT project. It is worth mentioning that, at the time this study was conducted, the high-lift devices of the SBW aircraft were not designed yet. Therefore, the present 'high-lift condition' refers to the clean wing operating at low speed and high angle of attack, close to its maximum lift coefficient.

The computational domain consisted of the volume between the aircraft, described in the previous section, and a sphere (VR0) placed at 35 fuselage lengths from the aircraft center. A sketch of this domain is shown in Fig. 1-(a). A far-field boundary condition was imposed on this sphere to simulate the flight condition indicated before. No-slip boundary conditions were applied to all solid surfaces. A turbulent wall model was used for all surfaces. On the propeller blades, where zig-zag trips were applied at 20% of the chord, the wall model is laminar before the trip and turbulent after it. Due to the symmetry of the case with respect to the Y plane, only half of the vehicle was simulated. An acoustic sponge region was specified, starting from a radius of 7.6ℓ from the aircraft center to damp outward-traveling and inward-reflected acoustic waves.

The computational domain was subdivided into 16 resolution regions (VRs). These regions were characterised by a constant grid size, which increased by a factor of 2 passing from consecutive VR levels. For simplicity and clarity of the drawing, only VR0, VR1, and VR9 are shown in the sketch in Fig. 1-(a), while finer VRs are shown in Fig. 1-(b). The finest region, VR15, where the voxel size was 1.37 mm and the physical timestep was $1.94e-06$ seconds, was defined as an offset of 6 voxels from the wing, the strut, and propeller blade surfaces. Subsequent regions, up to VR11, were defined as offset from the aircraft body to have higher resolution in the propeller wake and towards intersection regions between geometries, such as the strut-wing junction or the wing/strut-fuselage junction. The aforementioned offsets were defined such that 12 and 6 local voxels are placed between VRs 15 to 12 and VR 12 to 11, respectively. After that, VR10 was defined as a similar offset, but the distance between the previous VR was chosen to be large enough to

Table 2 Summary of computational setup parameters.

Description	Value
Number of VRs	16
Total cell count (M)	438.42
Finest cell size relative to the mean aerodynamic chord	$6.42 \cdot 10^{-4}$
Timestep relative to revolution period T	$3.5759 \cdot 10^{-5}$
Number of timesteps	335663
CPU hours	$6.903 \cdot 10^{4}$

include the FW-H surface, which will be described soon after. Following the description, VRs from 9 to 0 were defined as spheres distributed in space to have 24 voxels separating the neighboring regions in the radial direction. The FW-H analogy data was sampled on a permeable surface enclosing the aircraft, located inside VR10. Here, the mesh resolution allowed for recording fluid dynamic variables up to a cut-off frequency higher than 8 times the BPF. The permeable surface was defined as an offset from the aircraft plus a cylinder, which includes the propeller's wake, to reduce spurious noise sources arising from the interaction between the wake of the propeller and the FW-H surface. The FW-H surface and the virtual microphone array used in the noise directivity study are displayed in Fig. 3. Three equally shaped FW-H surfaces, placed 25 cm apart, were used to average noise signals. This averaging process allowed mitigating these spurious sources in the frequency range 2/3BPF - 4/3BPF [58], avoiding the need to neglect the exit face of FW-H surface and completely lose fundamental data to be used for the noise computation [59]. A dedicated region within VR11, encompassing the propeller blades and the spinner, was associated with a sliding-mesh local reference frame, indicated in Fig. 1-(b) as LRF, which rotated at the propeller angular speed with respect to the rest of the domain. To accelerate the convergence process, the simulations were performed using a coarse-to-fine approach. First, six rotor revolutions were simulated using a coarser mesh, and then the finer simulation was seeded using the coarse flow field. This procedure allowed the convergence time of the fine simulation to be reduced to two propeller revolutions. After convergence, data were collected on the FW-H surfaces for 10 rotor revolutions with a sampling frequency of 3214 Hz. The cost of one simulation for the installed case was around 70k CPU hours on 1024 cores on AMD EPYC 7H12 2.6GHz. Other relevant information about the numerical setup is reported in Table 2, and a grid convergence study is reported in Appendix .B.

V. Results

This section provides an overview of the installation effects before examining, in detail, their impact on aircraft aerodynamics and acoustics. Figure 4 shows an overview of the complex vortical structures in the strut-braced configurations. The image highlights the influence of the propeller slipstream on the aerodynamic characteristics of the wing by analyzing the isosurfaces of λ_2 colored by the magnitude of velocity normalized by the cruise speed. The

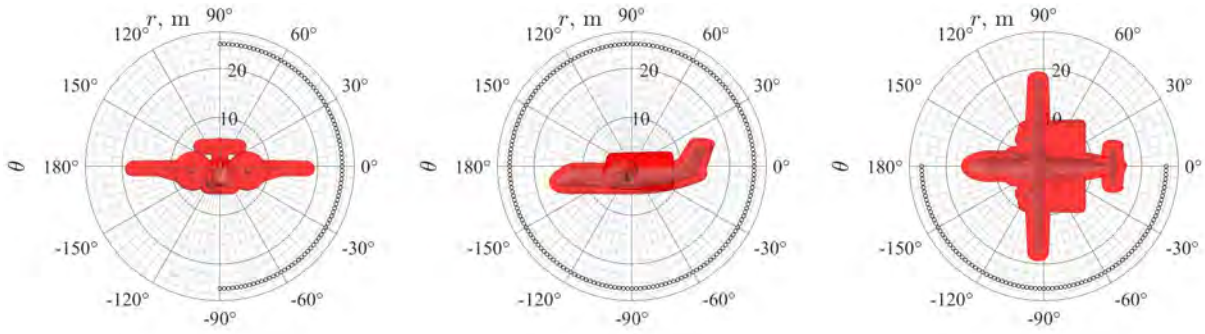

Fig. 3 Virtual microphone and FW-H permeable surface (in red) represented in the frontal plane (a), lateral plane (b), and aircraft top plane (c).

top-left inset illustrates variations in slipstream behavior between propellers rotating in opposite directions, while the top-right inset reveals a region of flow separation near the wing's trailing edge due to the interaction of tip vortices with the wing surface. These features are just a few of the intricate flow phenomena at play, which will be analyzed in detail in the following subsections.

The analysis begins with a discussion of global aerodynamic forces, followed by the description of the force distribution on the wing, strut, and blade surfaces. The wake dynamics are then explored, focusing on key interaction mechanisms that influence the wing and strut and their role in surface pressure fluctuations. Finally, the study compares aeroacoustic noise sources across different configurations and evaluates the aircraft's ground noise footprint under take-off conditions.

A. Effect on aircraft aerodynamic efficiency

This section discusses the installation effects on the aircraft's aerodynamic efficiency. Specifically, lift and drag are computed for each configuration and averaged over a rotor revolution. Figure 5 presents the aerodynamic efficiency (lift-to-drag) in the percentage of that for the propeller-off configuration, which corresponds to the aircraft configuration without the entire engine. The results show that the installation reduces aerodynamic efficiency by about 7% for the configuration with the propeller rotating inboard up and 8% for the one rotating outboard up. This finding aligns with results obtained by Chirico et al. [16] and Veldhuis [14], each reporting the advantages, in terms of aerodynamic efficiency, of employing the inboard up configuration on a cantilever wing. To gain a deeper understanding of the aerodynamic efficiency reduction, the next section will analyze the loading distributions on the wing and strut.

B. Effect on the strut-braced wing loading

In Fig. 6, the spanwise distributions of lift and drag are presented for the wing (a) and the strut (b). The quantities are expressed in terms of the parameters $\gamma_l = cC_l/(2b)$ and $\gamma_d = cC_d/(2b)$, where c is the local chord and b is the

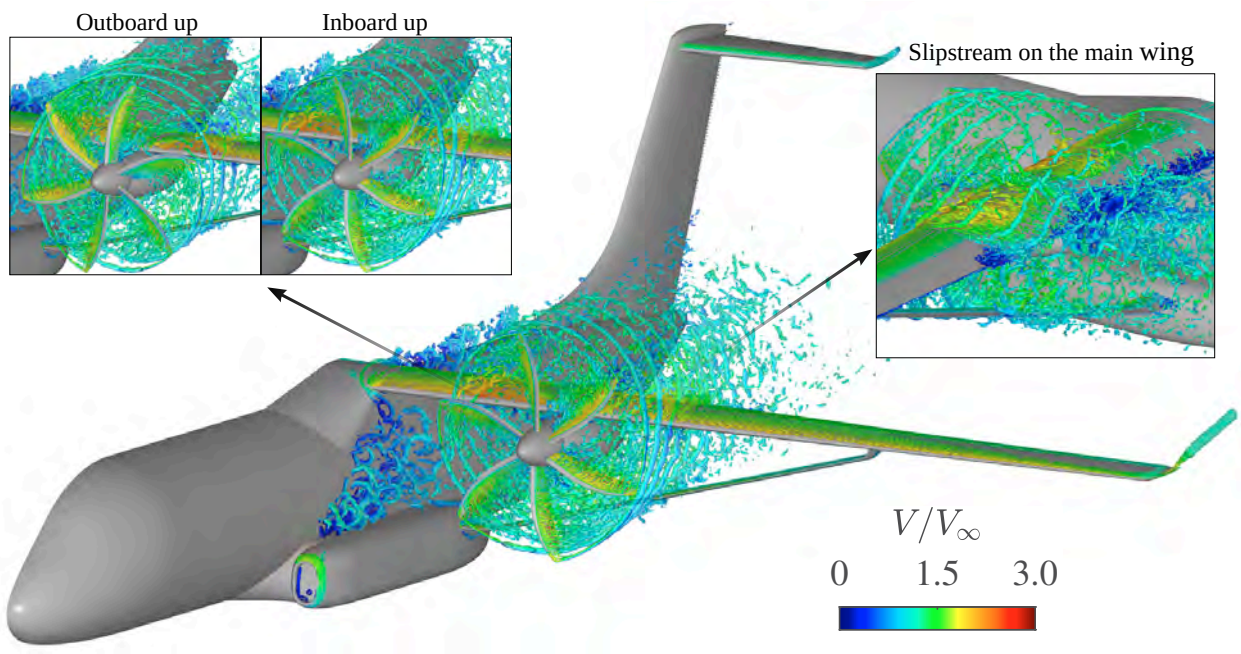

Fig. 4 Vortical structures around the aircraft (isosurface of λ_2 colored by the magnitude of velocity, V, normalized by the cruise speed, V_∞).

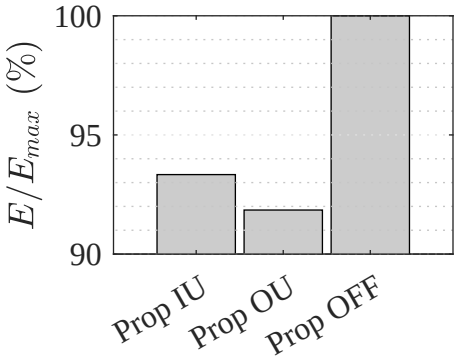

Fig. 5 Aerodynamic efficiency (lift-to-drag ratio) for different aircraft configurations.

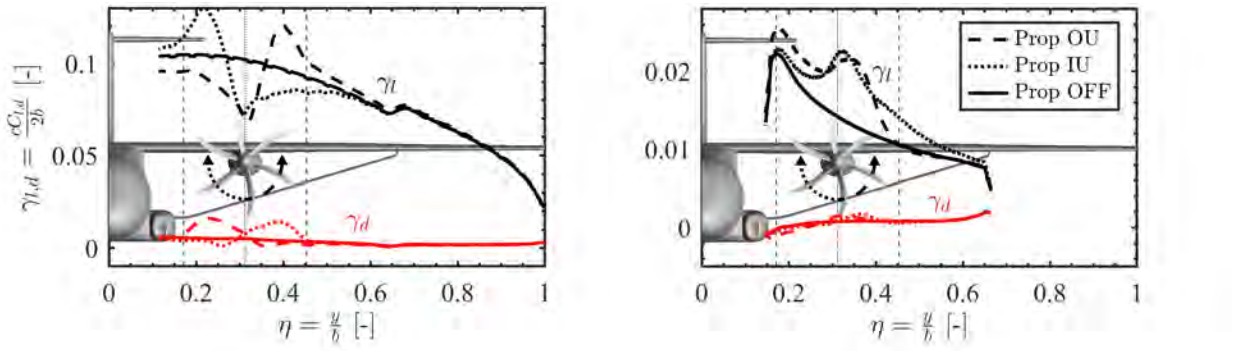

(a) *wing distribution* (b) *strut distribution*

Fig. 6 Span-wise distribution of lift, γ_l, and drag, γ_d, on the wing (a) and on the strut (b).

wing half-span. Continuous lines refer to the propeller-off configuration, whereas dashed and dotted lines refer to the configurations rotating inboard up and outboard up, respectively. This information is reported in the legend and also indicated by the arrows on the propeller.

Analyzing the results on the wing (Fig. 6-(a)), for both propeller-on cases, an increase in lift is observed on the upward side due to the increase in angle of attack induced by the slipstream, while a lift reduction is observed on the downward side. These results align with those shown by Refs [60, 61] for a cantilever wing. In particular, the propeller slipstream causes an increase in axial velocity seen by the wing sections behind the propeller and induces a swirl velocity component, which has a specular effect on the upward and downward sides. In addition, results show that the largest reduction in wing loading occurs at the propeller location ($\eta \approx 0.33$) due to the presence of the nacelle on the wing's pressure side. In the case without a nacelle, the spanwise location where the difference between the propeller-on and propeller-off wing loading changes sign (from a local increase to a local reduction in loading) is approximately at the propeller center. When the nacelle is present, the induced local minimum in wing loading at this position shifts the point at which there is a sign change towards the upward side of the wing.

When analyzing the wing drag distribution, γ_d, the propeller slipstream development tends to reduce the drag on the upward side and increase it on the other side. Indeed, although on the downward side, the wing generates less lift with respect to the configuration without the propeller, the change in effective angle of attack leads to an inclination of the lift vector in the direction of the flow and, therefore, to an additional component of drag induced by the propeller vorticity. The opposite happens on the upward side, leading to a local drag reduction with respect to the propeller-off configuration. It is worth mentioning that the drag reduction occurs with a markedly lower magnitude than its respective increment on the downward side, leading to an increase in the total wing drag of around 16.62% for the inboard up and 18.90% for the outboard up configuration. Given that the wing contributes the most to the aircraft's overall drag, this increase plays a significant role in the reduction of total aerodynamic efficiency observed in the previous section. This phenomenon appears to be linked to flow separation on the wing's suction side. This is illustrated in Fig. 7, which

presents averaged pressure coefficient contours along with black isolines indicating regions of reversed flow, as identified by the zero-value x-component of the skin friction coefficient (C_{f_x}). On the wing's upper side, three distinct separation regions, labeled A, B, and C, are observed:

- Regions A and B are outside the slipstream area and result from blade tip vortex interactions with the wing. The separated flow regions are similar for both propeller rotation directions.
- Region C, in contrast, appears only on the side where the propeller blades move from the pressure side to the suction side. As a result, it manifests inboard in the IU configuration and outboard in the OU configuration.

These three separated regions resemble the ones from the experimental findings of Duivenvoorden et al. [62], who observed similar reversed flow regions using oil flow visualization at high angles of attack. They also noted a span-wise movement and merging of the separation region C with the upward side separation (A in Fig. 7-(a) and B in Fig. 7-(b)). The authors hypothesized that this separation could be associated with a root vortex system, but lacked off-surface data to confirm this. In our simulations, we identified that the cause of the separation region C is a vortex originating from the nacelle, as shown in Fig. 8. This vortex is convected onto the upper wing surface, following the local flow pattern. Specifically, its movement is driven by a cross-flow (span-wise) component induced by the high-pressure gradient between the relatively low-pressure flow on the upward side and the high-pressure flow from the wing-nacelle junction. This pressure-driven convection pushes the vortex toward the slipstream boundary, explaining why the separation region C consistently occurs on the upward side, ultimately altering the expected drag distribution as previously described.

Examining the isolated strut in Fig. 6-(b), an overall increase in lift is observed, with minimal variation in drag. Specifically, total strut lift increases by 20.97% in the outboard up configuration and 24.68% in the inboard up configuration. Meanwhile, drag decreases by 7.57% in the OU case and approximately 1% in the IU case. Unlike the wing, where installation effects reduce aerodynamic efficiency, they have a positive impact on the strut's performance. Notably, while drag distribution remains almost unaffected by installation effects, the lift distribution, γ_l, exhibits significant variations that depend on the propeller's rotation direction. Specifically, the increase in axial velocity caused by the propeller leads the lift distribution to peak just behind the propeller for both installed configurations. Conversely, outside the slipstream, the strut lift loading is increased on the downward side while tending to the propeller-off distribution on the upward side.

C. Effect on blade loading

Following the previous section, which discussed the effect of the propeller on the wing loading, this section analyzes the impact of the wing on the propeller's blade loading.

Figure 9 shows the time history of thrust and torque coefficients over an entire rotor revolution, while, to simplify the discussion, Fig. 10 shows the blade thrust coefficient also as a function of the propeller azimuthal angle θ. In what follows, we will refer to the azimuthal angle in the Fig. 10-(a) as θ_{OU} and Fig. 10-(b) as θ_{IU}, respectively.

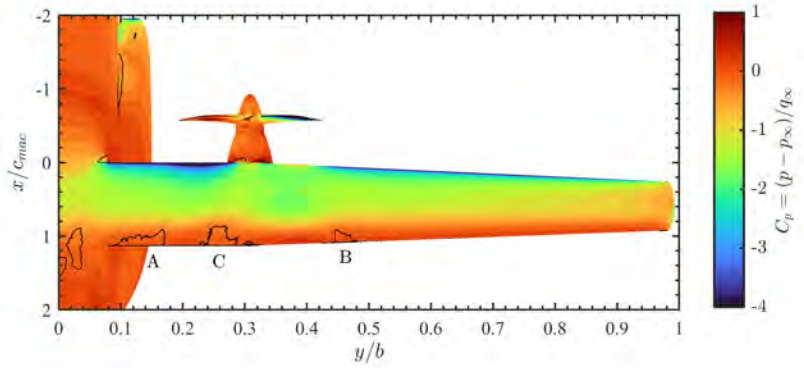

(a) *Inboard up*

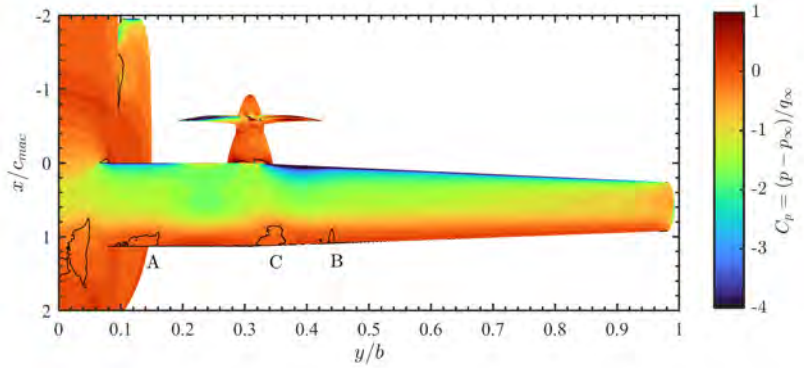

(b) *Outboard up*

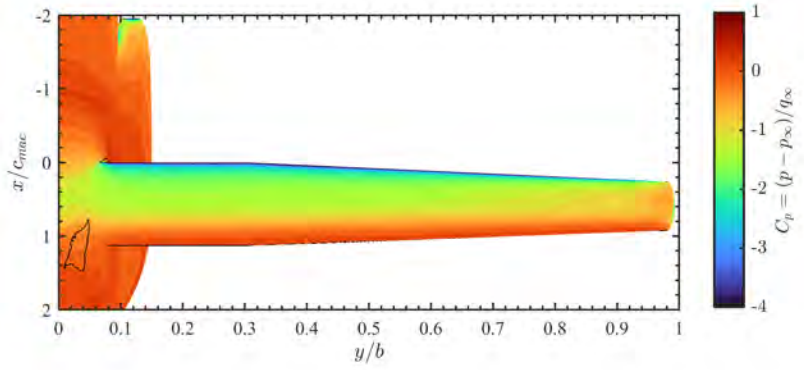

(c) *Without propeller*

Fig. 7 Pressure coefficient contours with $C_{f_x} = 0$ isoline (black) for (a) propeller rotating inboard up, (b) propeller rotating outboard up, and (c) no-propeller configuration.

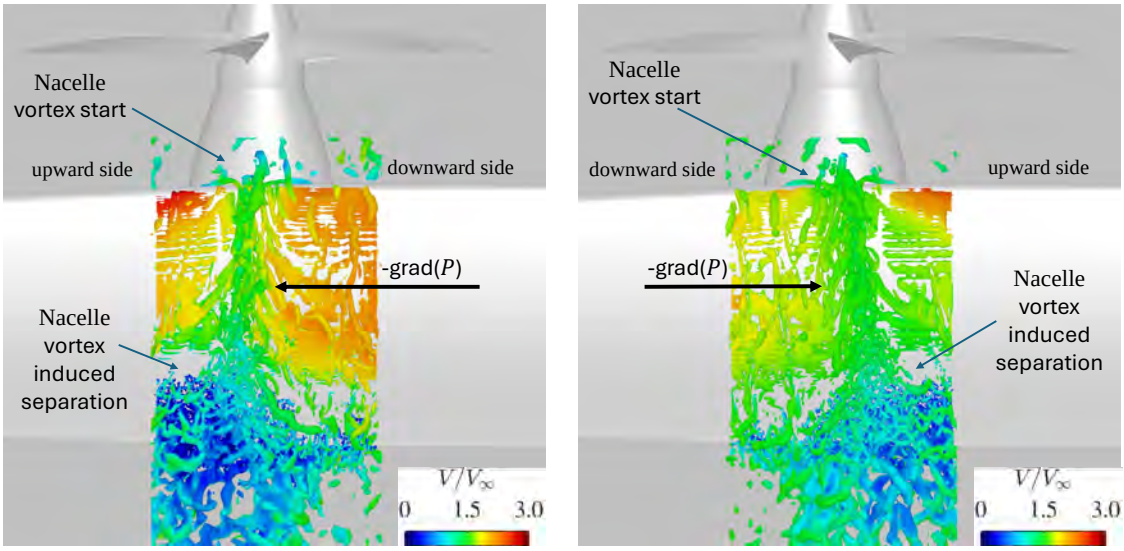

(a) Outboard up

(b) Inboard up

Fig. 8 Nacelle vortex visualization by means of isosurface of λ_2 colored with non-dimensional velocity magnitude, V/V_∞. Configuration with propeller rotating outboard up in (a) while rotating inboard up in (b).

In both the isolated propeller cases (solid line), a sinusoidal trend is observed: starting at $t/T = 0$ (corresponding to $\theta_{OU} = \theta_{IU} = 0°$), the force exerted by the blade decreases as the blade moves upward, reaching a minimum at $t/T = 0.25$ ($\theta_{OU} = 90°$ and $\theta_{IU} = 270°$). The force then increases as the blade moves downward, peaking at $t/T = 0.75$ ($\theta_{OU} = 270°$ and $\theta_{IU} = 90°$). This behavior is explained by the fact that the freestream flow is not aligned with the propeller axis. The vertical component of the freestream velocity ($V_\infty \sin(\alpha)$) reduces the effective angle of attack for upward-moving blades and increases it for downward-moving blades.

A similar pattern is observed in the installed configuration, but with some relevant differences. The presence of the wing modulates the temporal distribution of both thrust and torque, leading to larger temporal variations and an asymmetric load distribution with respect to the horizontal plane of the propeller ($\theta = 90°$). It is important to note that while the presence of the wing has little effect on the average thrust and torque values, i.e., lower than 3% (Table 3), it significantly affects the temporal behavior of these forces. This modification is crucial for aeroacoustic considerations, as this unsteadiness in the loading will contribute to higher far-field noise. In addition, the asymmetry in the blade loading over a revolution will amplify the tones at harmonics of the blade passing frequency, as discussed in Section V.F.

To understand the causes of this difference, an inspection of the radial elementary blade loading, dC_T, is necessary. In Fig. 11, the difference in radial blade loading between the installed and isolated cases

$$\Delta\left(\frac{dC_T}{d\bar{r}}\right) = \frac{dC_T}{d\bar{r}}_{installed} - \frac{dC_T}{d\bar{r}}_{isolated} \tag{5}$$

Table 3 Blade forces variation between the installed configuration and the isolated propeller case.

	Inboard up		Outboard up	
	ΔC_T (%)	ΔC_P (%)	ΔC_T (%)	ΔC_P (%)
SBW	2.45	1.28	1.59	0.70
CNT	3.19	1.80	2.39	1.26

is shown versus the azimuthal angle θ. Focusing on the configuration rotating outboard up, Fig. 11-(a), two distinct regions are identified: 1) a region of load increase in the fourth quadrant (Q4 in the image) between 60% and 90% of the blade span, with a peak at around 80% of the span and an azimuthal angle of $\theta \approx 275°$, which corresponds to the maximum location of thrust shown in the graphs in Fig.10-(a) (black filled dot) and 2) a region of load reduction in the second quadrant (Q2 in the image) between 45% and 70% of the blade span, with a peak of reduction at around 60% of the blade span and an azimuthal angle of $\theta \approx 150°$ (which location is advanced in the rotation with respect to the location of minimum thrust shown with unfilled symbol in Fig. 10-(a)). The identification of these two regions is associated with the wing's bound vorticity [14], which generates two key effects: (i) an upwash, which increases the angle of attack for the blades moving from the suction to the pressure side (Q3 and Q4) and reduces it for the ones moving in the opposite direction (Q1 and Q2). And (ii) an axial velocity variation that reduces the angle of attack for blade elements located on the wing suction side (Q2 and Q3) and increases it for those moving on the wing pressure side (Q1 and Q4). These two effects combine to increase the blade loading in Q4 and reduce it in Q2, leading to the observed asymmetry in the loading distribution. Same consideration holds for the inboard up configuration, Fig. 11-(b), but in quadrants Q1 and Q3, respectively.

Figures 9 and 10 present the blade thrust and torque also for the case of the tube-and-wing configuration (CNT). It can be seen that, due to the strut's relatively small size and lower aerodynamic load compared to the main wing, its effect on blade loading can be considered negligible, and indeed Table 3 reports less than 1% difference between the cantilever and strut-braced wing cases for all the configuration analyzed. It is important to note, however, that this result is design-specific and depends strongly on the level of aerodynamic loading on the strut compared to that on the wing. Therefore, it cannot be generalized to all SBW configurations but only to those featuring a lightly loaded strut element. A dedicated study on the influence of the ratio between the wing and strut loading on the propeller aerodynamics would be valuable to further assess this effect.

D. Wake dynamics

This section describes the dynamics of the propeller wake and its interaction with the wing behind. Overall, the wake generated from the propeller blades forms a helicoidal structure that impinges on part of the wing and the strut behind it. The flow field is visualized in Fig. 12, where isosurfaces of λ_2 are shown. In general, the instantaneous

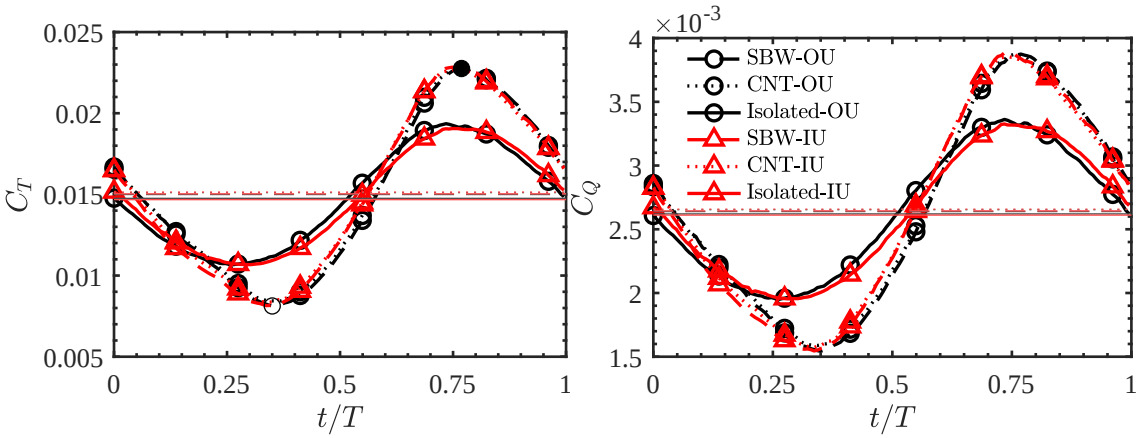

(a) (b)

Fig. 9 Thrust (a) and torque (b) coefficient exerted on one propeller blade over a full revolution. The displayed data are obtained by phase averaging of 10 revolutions.

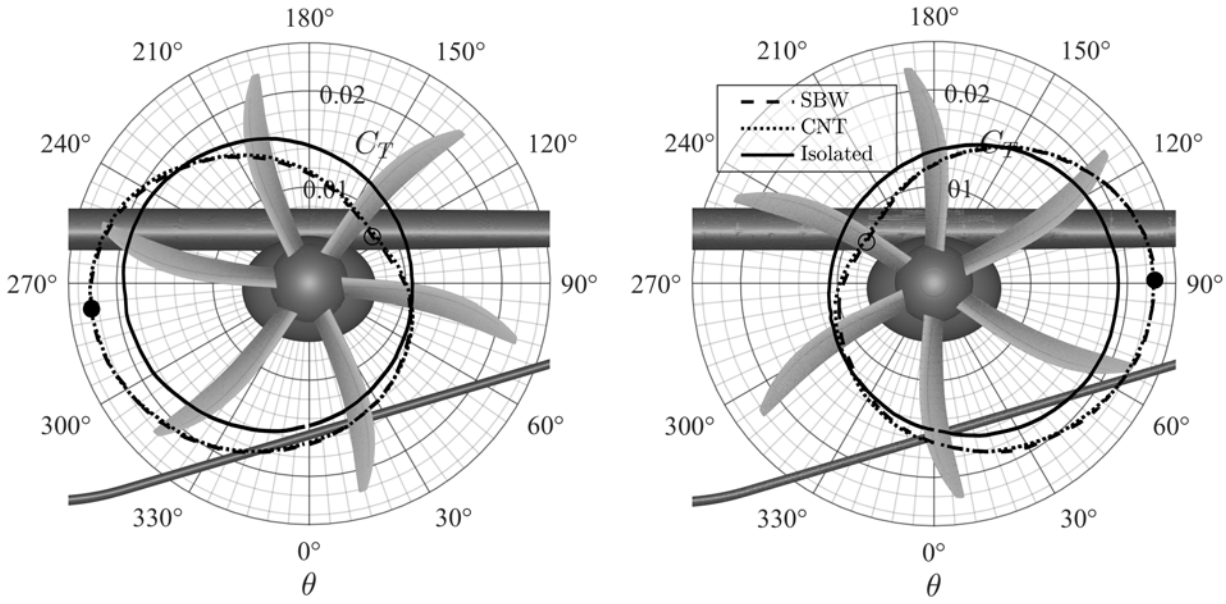

(a) *Outboard Up* (b) *Inboard Up*

Fig. 10 Thrust coefficient exerted on one propeller blade over a full revolution in the propeller angular reference frame. The displayed data are obtained by phase averaging of 10 revolutions.

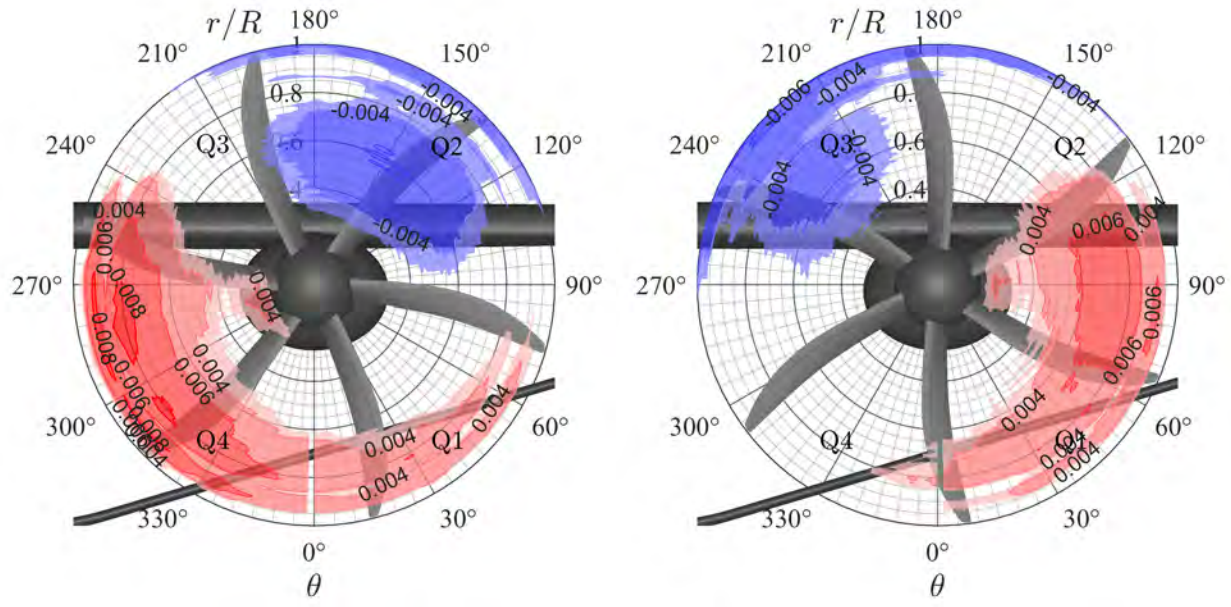

(a) *Outboard Up* (b) *Inboard Up*

Fig. 11 Map of the difference between the blade radial loading in installed condition and the blade radial loading in isolated condition during one rotor revolution. Data are obtained by phase averaging of 10 revolutions. Values of the difference between ± 0.003 are intentionally left out for clarity of the figure.

vorticity fields shown are included to illustrate the impingement mechanism. The statistical effects of the interaction are instead quantified through the analysis of pressure power spectra and of the phase-averaged removed surface pressure fluctuations shown in section V.E.

The wake development along the longitudinal direction can be observed in Fig. 13 where the out-of-plane vorticity is shown in the propeller vertical plane. From this figure, it is evident that the wake retains a well-defined structure before reaching the wing ($x/c_{mac} < 0$) and in the initial phase of its interaction with the wing ($x/c_{mac} < 1$). During these phases, two primary vortical structures are identifiable: the tip vortex and the trailing vorticity. These structures have distinct effects during the interaction, which will be discussed in greater detail in section V.E, particularly concerning their impact on pressure fluctuations on the wing and strut surfaces. As the wake progresses downstream ($x/c_{mac} > 1$), the suction side and pressure side flow branches interact with the vortical structures generated by the nacelle, resulting in a more chaotic wake pattern. This behavior resembles the interaction between the hub vortex and tip vortex observed by Posa et al. [17] in the far wake of a marine propeller–rudder system. Additionally, due to the non-axial inflow, the slipstream tube (indicated by the gray dashed lines in Fig. 13) is inclined approximately at the propeller's angle of attack relative to its axis. While this inclination has minimal impact on the wake-wing interaction, it plays a crucial role in the strut's wake dynamics. In fact, a different wake inclination could significantly alter the strut's interaction mechanism, as will be discussed later.

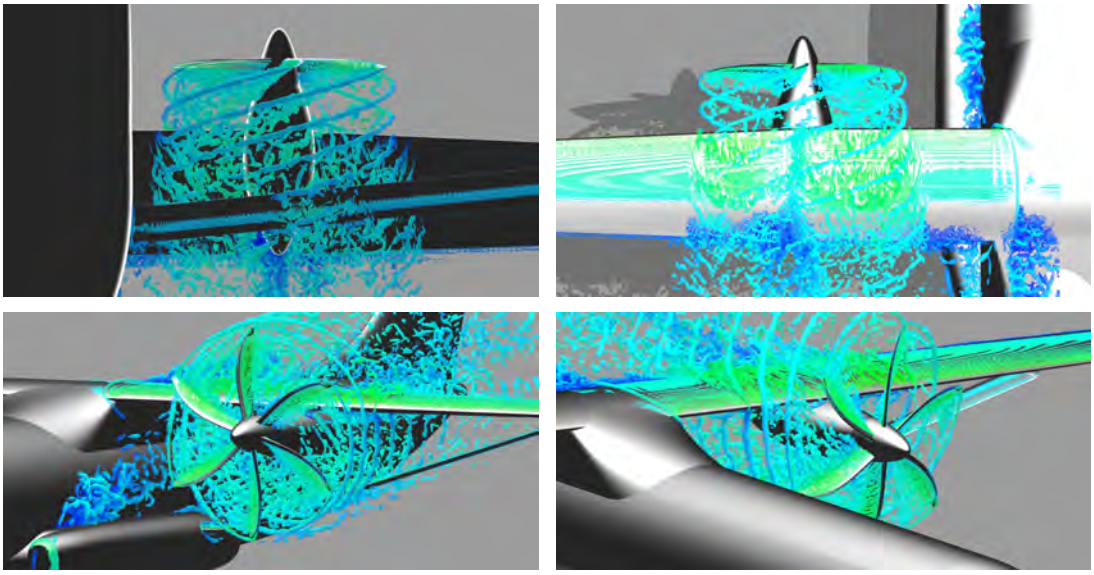

Fig. 12 Propeller wake development for the strut-braced configuration with the propeller rotating outboard (isosurfaces of λ_2). The top-left image shows the interaction of the propeller wake with the strut and the wing's pressure side. The top-right inset highlights the interaction between the propeller wake and the wing's suction side. The bottom-left and bottom-right images illustrate the development of the tip vortex as it bends around the wing's leading edge while moving downstream.

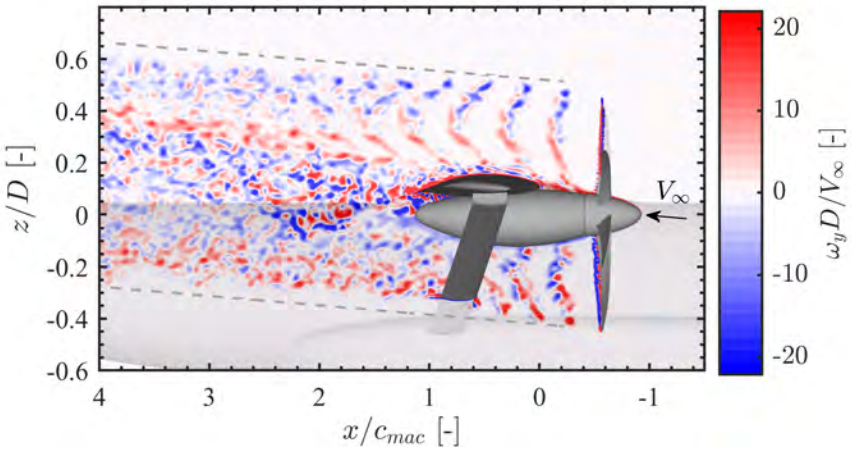

Fig. 13 Contour of non dimensional y-vorticity (out-of-plane) component, $\omega_y D/V_\infty$, in the propeller middle plane.

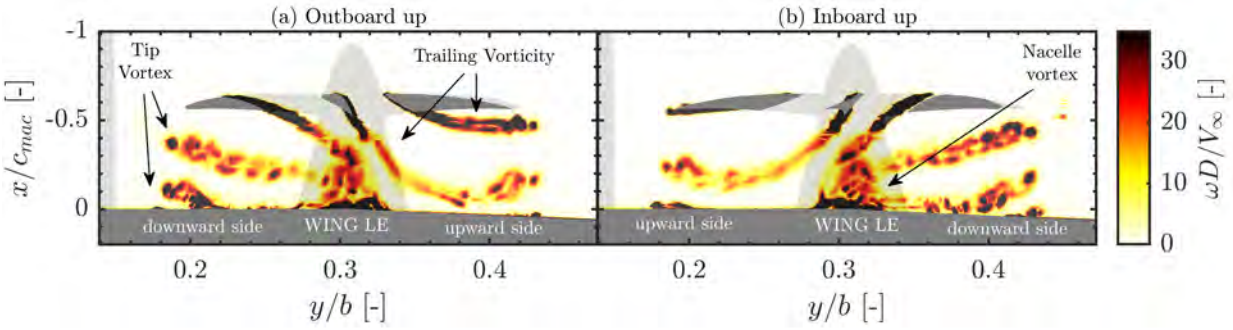

Fig. 14 Contour of instantaneous non-dimensional vorticity magnitude, $\omega D/V_\infty$, in the chord plane of the main wing.

To facilitate the discussion, we divide the interaction into three phases: (1) the approaching phase, when the propeller wake is moving towards the wing; (2) the interaction phase, when the propeller wake comes through the wing surface, interacting with its boundary layer and (3) the convection phase, after the wake passes the wing and travels far behind.

In the approach phase, two distinct interaction mechanisms are observed on the wing and the strut. Firstly, the tip vortices impinge on the LE of the wing at the edges of the slipstream region, whereas the trailing vorticity encounters the wing on the inner part. As can be observed in Fig. 14, the tip vortex approaches the wing with an initial circular core and starts deforming its shape and size in a similar way to what was observed experimentally by Felli [30] and numerically by Posa et al [17]. Specifically, when the vortex is approximately one initial vortex core size, σ_0, distant from the wing, its shape deforms into an elliptic-like shape with the major axis aligned to the wing LE, its size reduces due to the interaction with the wing boundary layer and the vortex itself moves away from the propeller axis of about $1.5\sigma_0$ before the following vortex starts interacting with the wing LE. The process repeats with a frequency equal to the blade passing frequency on both downward and upward sides. It can be explained, with the image vortex model, as the effect of the induced velocity caused by an equal and opposite vortex located on the wing LE.

Additionally, a marked vorticity spot can be observed in the center of the slipstream. This spot is caused by a vortex that starts from the nacelle and moves on the wing's upper side, following the pressure gradient between the low-pressure region on the upward side and the high-pressure flow from the nacelle. This phenomenon contributes to flow separation, whose impact on wing loading was discussed in the previous section. Finally, similar behaviors are observed in the configurations rotating inboard up and outboard up, respectively.

To describe the approach phase of the propeller wake on the strut, we examine the trace of the propeller slipstream on the strut's chord plane. Specifically, a contour of instantaneous vorticity magnitude is shown in Fig 15. The approach phase starts when a blade first intersects this plane (points A in Fig.15). Then, the combination of propeller rotation and convection velocity leads to the oblique shape traces observable by the trace of vorticity shed by the previous blade. A clear distinction between tip and trailing vorticity is present at the first stages of the approach phase. As mentioned before, when the wake is convected downstream, the vortical tube moves upward to follow the freestream flow. This

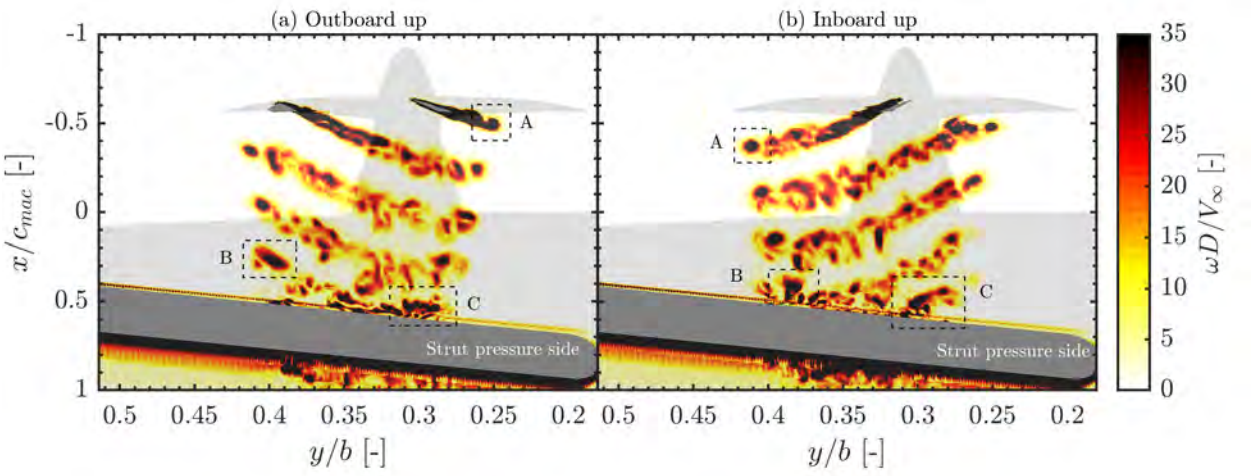

Fig. 15 Contour of instantaneous non-dimensional vorticity magnitude, $\omega D/V_\infty$, in the chord plane of the strut.

vertical motion tends to reduce the span-wise elongation of the vortex trace in the strut chord plane since now the interaction involves only a lower arc of the wake tube. Therefore, close to the LE of the strut, the tip vortex impingement mechanisms differ from the one observed on the wing. Indeed, while on the wing, this impingement can be modeled as an almost orthogonal vortex, on the strut, the tip vortex impinges almost parallel to it. This is even clearer when looking at the more elongated tip vortex traces highlighted in boxes B and C in Fig. 15. Again, similar behaviors are observed in the configurations rotating inboard up and outboard up, respectively.

E. Effect of wake impingement on surface pressure

The impingement of the propeller wake on downstream components is generally the cause of high pressure fluctuations on their surfaces. These fluctuations arise from both the periodic passage of the blades and the broadband turbulent motions within the wake. To characterize them, two complementary analyses are performed on the same pressure field. First, we examine the pressure power spectrum at integer multiples of the blade-passing frequency (BPF). This analysis, here referred to as the *tonal part*, highlights the frequencies where the coherent blade-related content is most pronounced, although broadband energy is still present at all frequencies. For this purpose, the zero-mean pressure signal

$$\tilde{p}(t) = p(t) - \overline{p}, \qquad \overline{p} = \frac{1}{T_{\text{rec}}} \int_0^{T_{\text{rec}}} p(t)\, dt, \tag{6}$$

is used to compute the power spectrum, from which we extract the levels at the first few harmonics of the BPF. Second, to emphasize the fluctuations not coherent with the propeller rotation, we compute the phase-averaged pressure,

$$\langle p \rangle_{pa}(t) = \frac{1}{N_p} \sum_{k=0}^{N_p-1} p(t + kT), \qquad t \in [0, T], \tag{7}$$

and define the residual field $p''(t) = p(t) - \langle p \rangle_{pa}(t)$. This residual represents the so-called *stochastic part*, which includes the broadband and random contributions after the removal of the periodic blade motion.

Figure 16 presents the spectral maps at multiples of the BPF on the wing for the outboard up configuration; the trends for inboard up are analogous and therefore omitted for brevity. Panels (a–e) and (f–j) correspond to suction and pressure sides, respectively, with columns indicating successive BPF harmonics as indicated in the column headings. The largest amplitudes occur at the first BPF and decrease with increasing harmonic order. Up to the third harmonic, streak-like features are visible on both sides of the wing, generated by the passage of the propeller tip vortex along the surface. Beyond the third harmonic, the coherent fluctuations lose importance, and the spectral distribution resembles that of the stochastic field, shown in Fig. 17-(a). Two distinct patterns can be observed: tip-vortex impingement produces edge lobes elongated in the chordwise direction due to the longer interaction time with the surface, while trailing-vortex impingement results in a broader, more uniform region closer to the wing LE. The trailing-vortex-induced fluctuations are stronger on the upward side, likely due to the higher local expansion, while the tip-vortex imprint extends further chordwise on the downward side (see $f/BPF = 3$, Fig. 16-(c) and (h)). This behavior is consistent with the higher blade loading on that side, which translates into a larger vortex core and higher vortex intensity. Figure 17 shows the residual RMS field p''_{rms} (stochastic part) for both OU and IU configurations. The imprint of both tip and trailing vortices remains visible, although the intensity difference between the upward and downward sides is now less pronounced. The stochastic field highlights the regions affected by flow separation induced by the nacelle and by the tip-vortex interaction near the trailing edge.

Regarding the strut, Fig. 18 and 19, the distinction between the tip and trailing vorticity contributions is less evident than for the wing because of the different type of wake-body interaction. Nevertheless, lobes associated with the tip-vortex impingement can still be identified, as highlighted by the boxes in Fig. 19. These lobes are noticeably wider than those observed on the wing, since the wake interacts with the strut through a tip vortex impinging almost parallel to the strut LE. The spectral levels exhibit the highest amplitudes at the first BPF and progressively decrease with increasing harmonic order. No clear difference is observed between the upward and downward sides, and no streak-like features appear along the surface. At higher f/BPF, the shape of the pressure power distribution increasingly resembles that of the stochastic field shown in Fig. 19. The stochastic map does not display the tip-vortex-related lobes but rather a region of nearly constant chordwise extent, whose spanwise size is smaller than that observed on the wing because of the strut's position relative to the propeller. Despite its reduced overall dimensions, the comparable intensity of the induced pressure fluctuations suggests that the relative importance of the wake–strut interaction may be significant. Further investigation is needed to assess the resulting structural response and possible vibration effects.

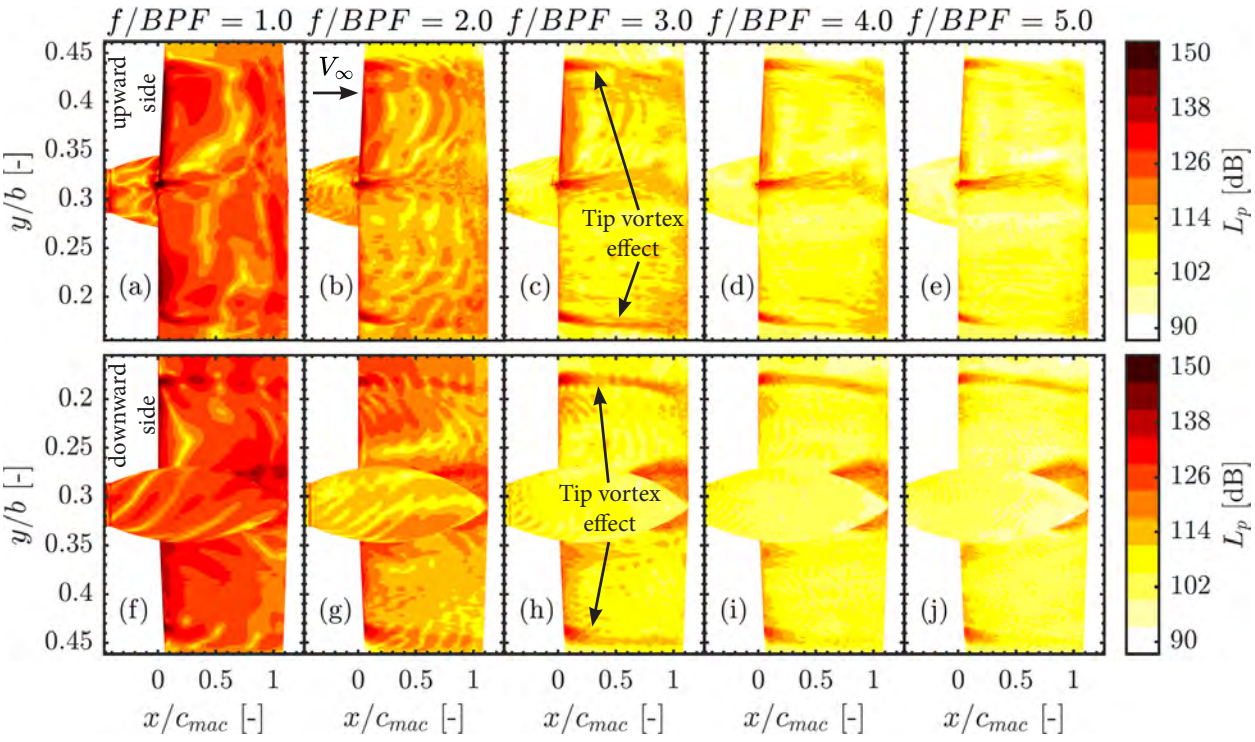

Fig. 16 Spectral maps of the surface pressure fluctuations on the wing for the outboard up configuration. Panels (a–e) and (f–j) correspond to the suction and pressure sides, respectively. Each column shows the power spectral level at successive harmonics of the blade-passing frequency (BPF).

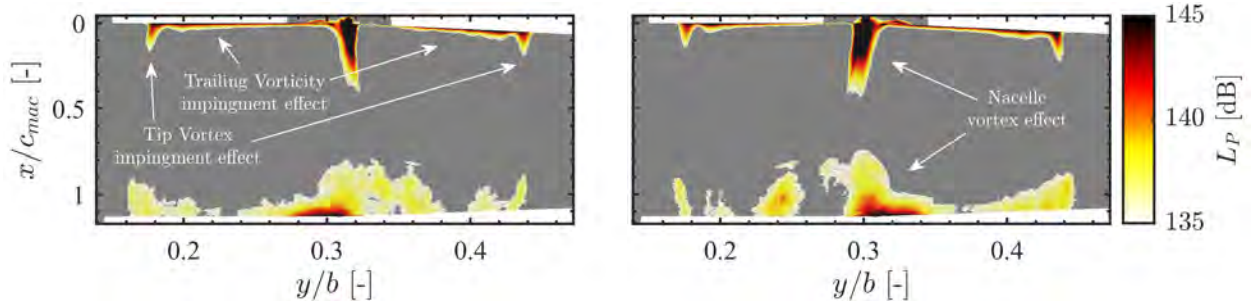

(a) Outboard up

(b) Inboard up

Fig. 17 Residual RMS field of the surface pressure fluctuations on the wing suction side, obtained by removing the phase-averaged pressure from the instantaneous field. Flow is directed toward positive x/c_{mac}.

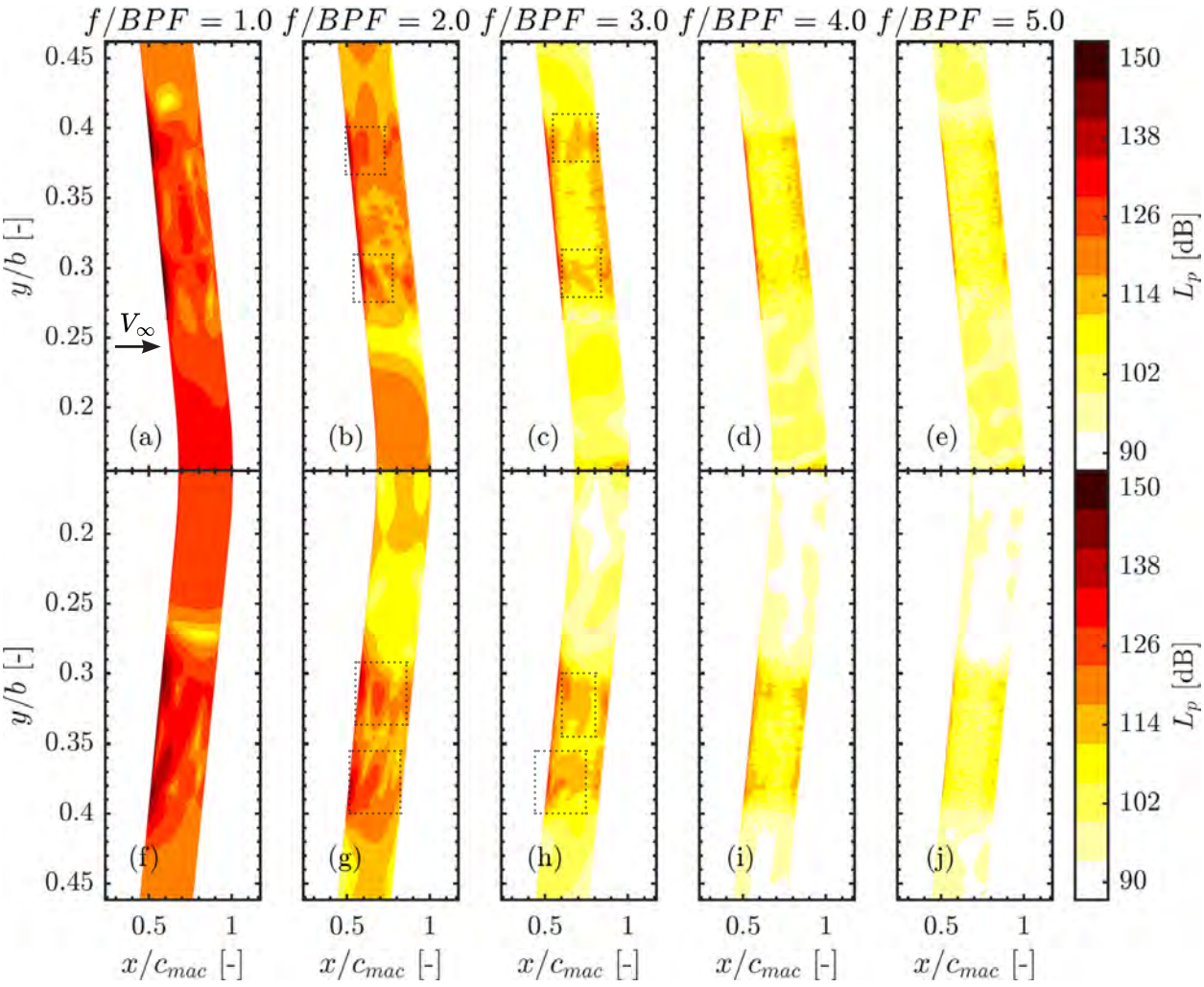

Fig. 18 Spectral maps of the surface pressure fluctuations on the strut for the outboard up configuration. Panels (a–e) and (f–j) correspond to the suction and pressure sides, respectively. Each column shows the power spectral level at successive harmonics of the blade-passing frequency (BPF).

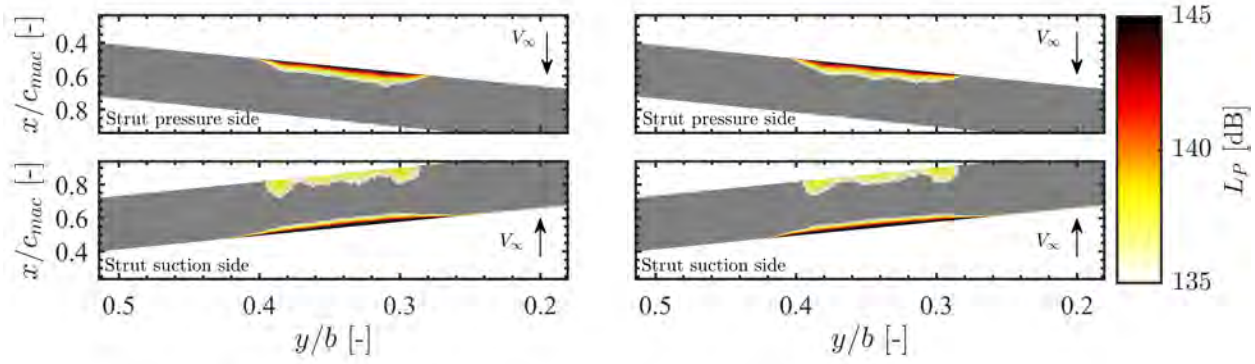

(a) Outboard up

(b) Inboard up

Fig. 19 Residual RMS field of the surface pressure fluctuations on the strut, obtained by removing the phase-averaged pressure from the instantaneous field.

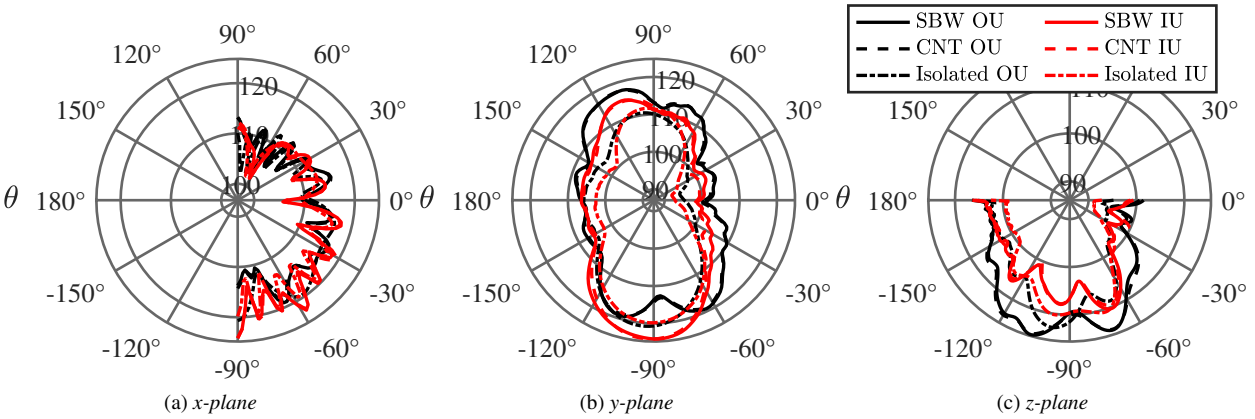

(a) *x-plane* (b) *y-plane* (c) *z-plane*

Fig. 20 OSPL directivity comparison in the aircraft's frontal plane (a), aircraft's symmetry plane (b) and aircraft horizontal plane (c)

F. Effect on far-field noise

To conclude the analysis, installation effects on the aircraft's far-field noise emission are presented. Permeable formulation of the Ffowcs-Williams and Hawkings analogy implemented in the frequency domain is used to estimate the noise at virtual microphones. More information about the method used and the FW-H surface employed can be found in Section III. Additionally, in Appendix .C, the prediction obtained with the hybrid CAA solver is validated against direct noise computation extracted from the flow field. In the following, a sound directivity analysis is presented, followed by an on-ground footprint assessment for take-off conditions to evaluate the impact of the observed trends on aircraft certification.

1. Directivity

The analysis has been performed by looking at the Overall Sound Pressure Levels (OSPL) directivity in three characteristic planes of the aircraft, namely the frontal (Fig. 20-(a)), symmetry (Fig. 20-(b)) and horizontal planes (Fig. 20-(c)). These planes and the microphone distribution are also shown in Fig. 3.

Before diving into the discussion of OSPL and directivity changes, it is worth mentioning that the installed propeller system is acoustically non-compact. Specifically, the wavelengths of the sound produced by the propeller, already at the first BPF ($\lambda = 3.14$ m), are smaller than the fuselage diameter. This leads to complex interactions between the sound waves and the surrounding geometry, which can significantly affect the resulting sound propagation.

Focusing first on the OSPL directivity in the frontal plane (Fig. 20-(a)), a similar trend can be observed among all the configurations analyzed, characterised by an irregular curve shape and higher emissions in the bottom direction ($\theta = -90°$). In the aircraft's symmetry plane (Fig. 20-(b)), the isolated propellers show an almost dipolar distribution, either for the inboard up and outboard up configuration, with main lobes at $\theta = \pm 90°$ and minimum sound levels at $\theta = 0$ and $180°$. By inspecting the noise spectrogram (Fig. 21, third column), one can observe that these main lobes

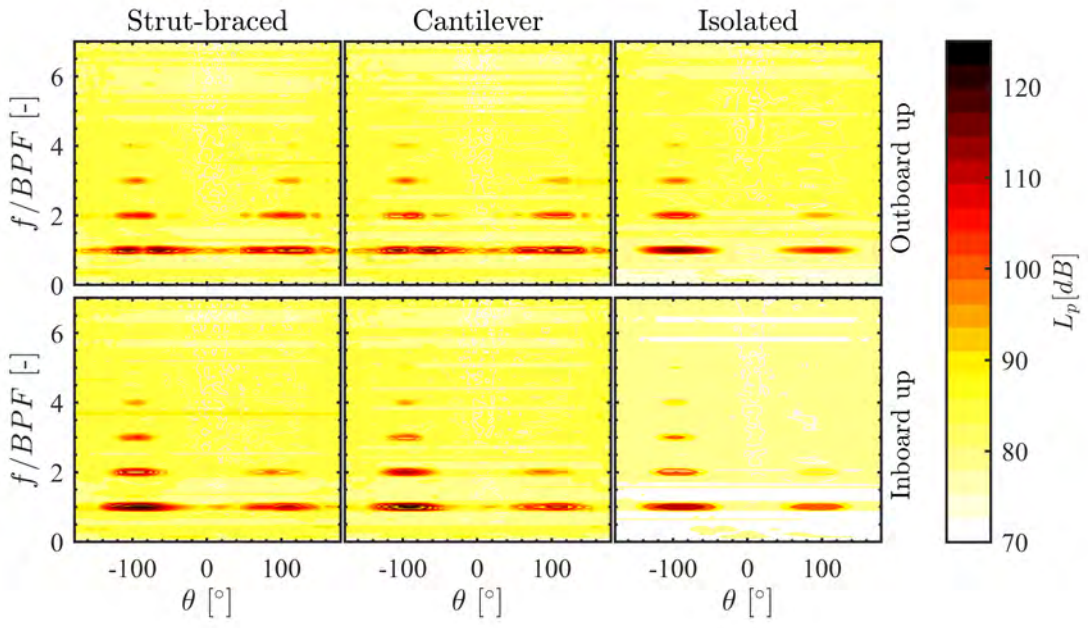

Fig. 21 Noise spectrograms showing sound pressure levels (L_p) across frequencies normalized by the blade passing frequency (BPF) and microphone angles θ for the aircraft's symmetry plane (y-plane).

show pronounced tones at the blade passing frequency, with an asymmetry between the upper and lower sides in both the amplitude and the number of distinct harmonics. This asymmetry is caused by the non-zero inflow angle and is in line with previous results obtained in literature [63, 64]. Outside these main lobes, no tonal contribution is observed due to destructive interference between the two propellers.

Compared to the isolated case, in the installed configurations we observe two main differences: an overall increase of the OSPL and a slight modification of the directivity pattern. The increase in OSPL manifests itself as an increase in the BPF tones' amplitudes and with a higher distinct number of harmonics. For instance, in the inboard up case, a 4^{th} BPF tone and a 2^{nd} BPF tone are shown in angular positions, which are not reported in the respective isolated case. Such an increase in OSPL can be attributed to the modification of the blade loading caused by the wing-bound vorticity, as observed in Section V.C. Conversely, the modification in directivity shape results from sound wave reflections on nearby geometries, transforming the directivity pattern into a multi-polar distribution. Interestingly, this phenomenon induces a destructive effect at the microphones located around $\theta = -90°$ for the installed configurations rotating outboard up, showcasing a minimum in the OSPL curves in Fig 21-(b) and localized reduction of the 1^{st} BPF tone in Fig. 21 (first row). To investigate the cause of this reduction, dilatation fields in the frequency range $1/4 < f/BPF < 4$ are shown in Fig. 22. Here, we can observe that, for the inboard up configuration (b), the waves propagate from the blades to the ground during the downstroke. The sound coming from the two propellers constructively interferes with each

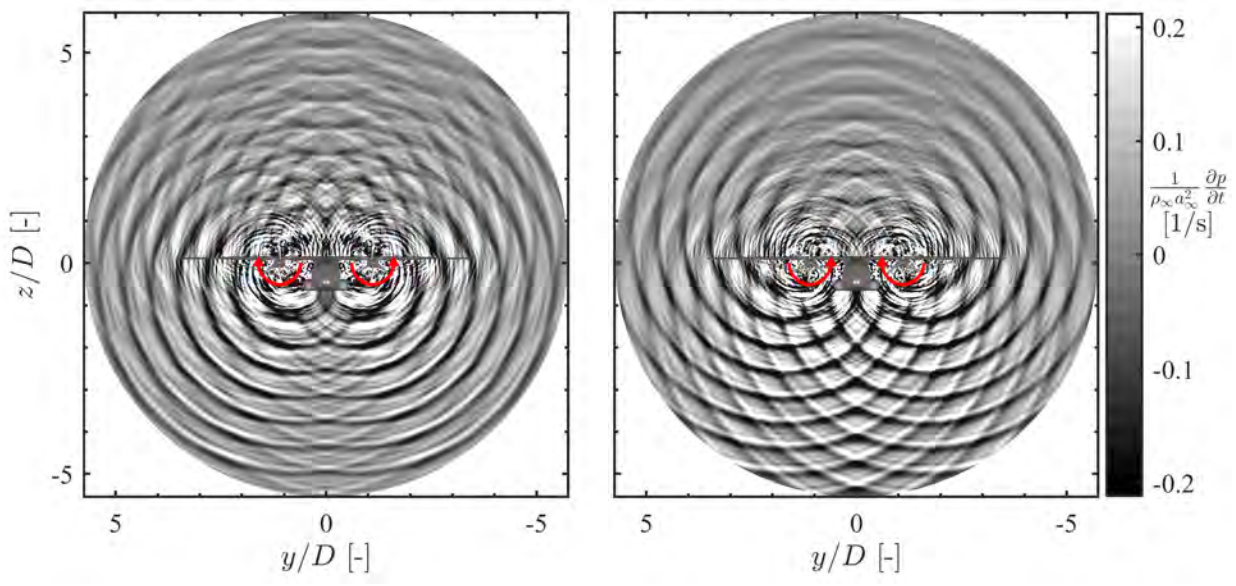

(a) *Outboard up* (b) *Inboard up*

Fig. 22 Dilatation field on a plane positioned 1.5 **propeller radius behind the center of the propeller in the aircraft frontal view. Data extracted from direct CFD results in the range** $1/4 < f/BPF < 4$**. Configuration with propeller rotating outboard up in (a) while rotating inboard up in (b).**

other, leading to the OSPL peak at $\theta = -90°$ observed in Fig. 20-(b). On the contrary, for the outboard-up installed configuration, Fig. 22-(a), the fuselage sponson acts as an obstacle, obstructing the wave propagation towards the ground. That causes the local minimum at $\theta = -90°$ in Fig. 20-(b) and generates higher levels of pressure fluctuation on the fuselage of the outboard up configuration, compared to the inboard up, at the first BPF (see Fig. 23).

Finally, the horizontal plane directivity, Fig. 20-(c), shows that, in the aircraft centre-line ($\theta = 0$ and $180°$), the isolated configuration presents the lowest contribution due to destructive interference between the two propellers. Then, the OSPL increases moving towards the center of the array. The installed cases show a similar directivity shape compared to their respective isolated case, with the configuration outboard up exhibiting overall higher levels of sound. Spectrograms in Fig. 24 show that this increment manifests with higher amplitudes of the BPF tones. Conversely, a decrease in OSPL is observed between $\theta = -80°$ and $-120°$ for the inboard up configuration. This can be again associated with on-body reflections that cause a crucial rule for wave propagation, as can be understood by looking at the differences between the dilatation fields for the outboard up Fig. 25-(a) and for the inboard up configuration (b).

Across all operating conditions, the cantilever and strut-braced configurations exhibit very similar OSPL distributions (Fig. 20). The spectral directivity maps in Fig. 21 also show that the two configurations produce very similar spectral patterns. In these maps, the small differences induced by the strut are not easily identifiable because they are confined to a narrow frequency range and are masked by the dominant tonal contributions. Therefore, to better illustrate these

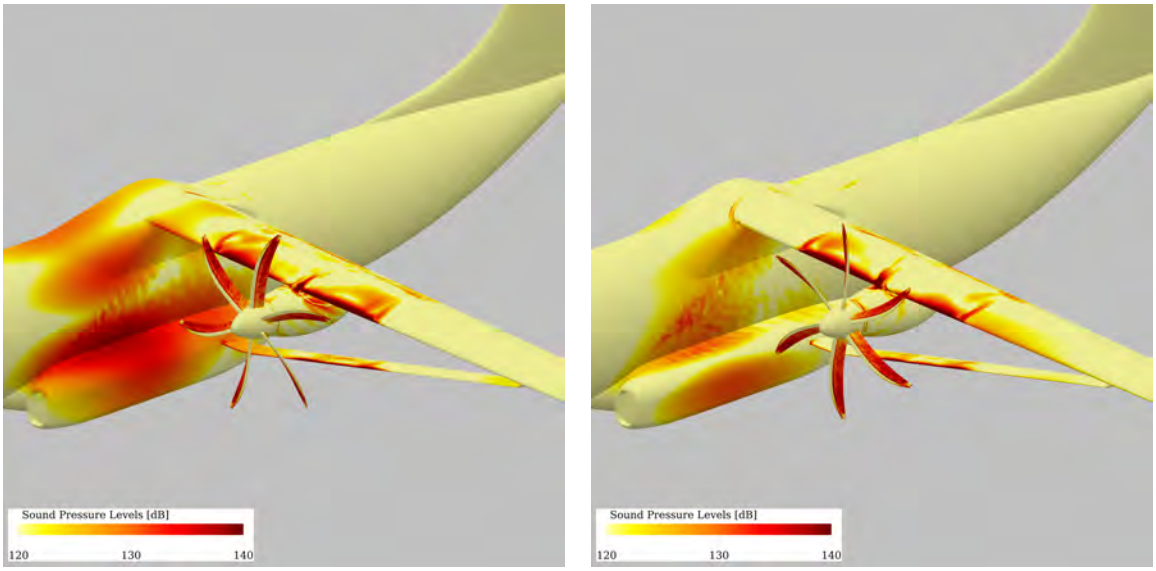

(a) *Outboard up* (b) *Inboard up*

Fig. 23 Sound pressure levels at the 1^{st} BPF on the aircraft surface. Data extracted from direct CFD results. Configuration with propeller rotating outboard up in (a) while rotating inboard up in (b).

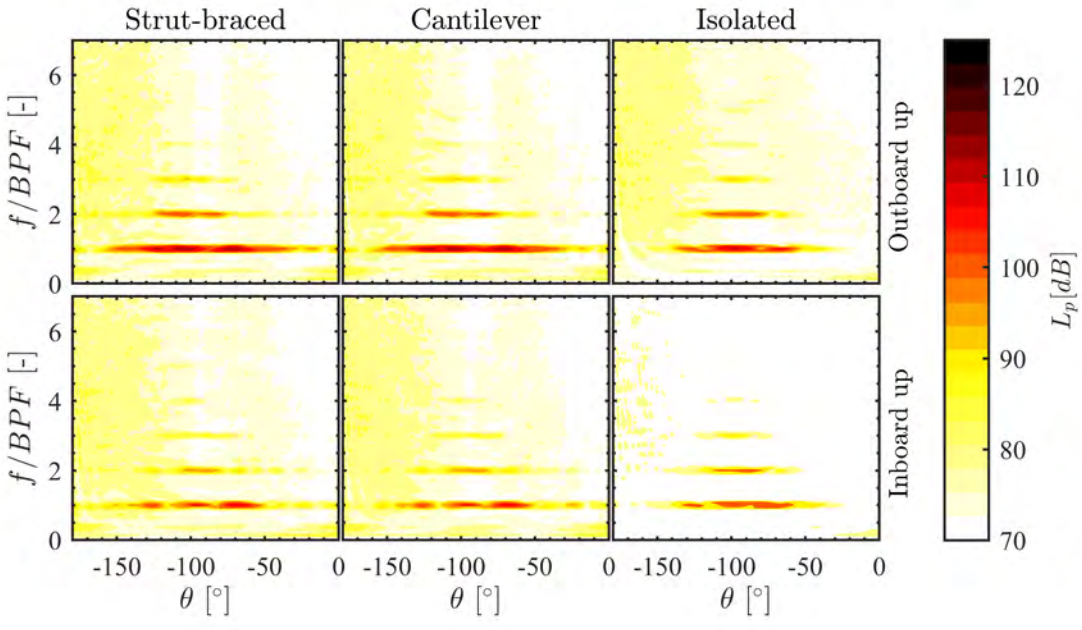

Fig. 24 Noise spectrograms showing sound pressure levels (L_p) across frequencies normalized by the blade passing frequency (BPF) and microphone angles θ for the aircraft's horizontal plane (z-plane).

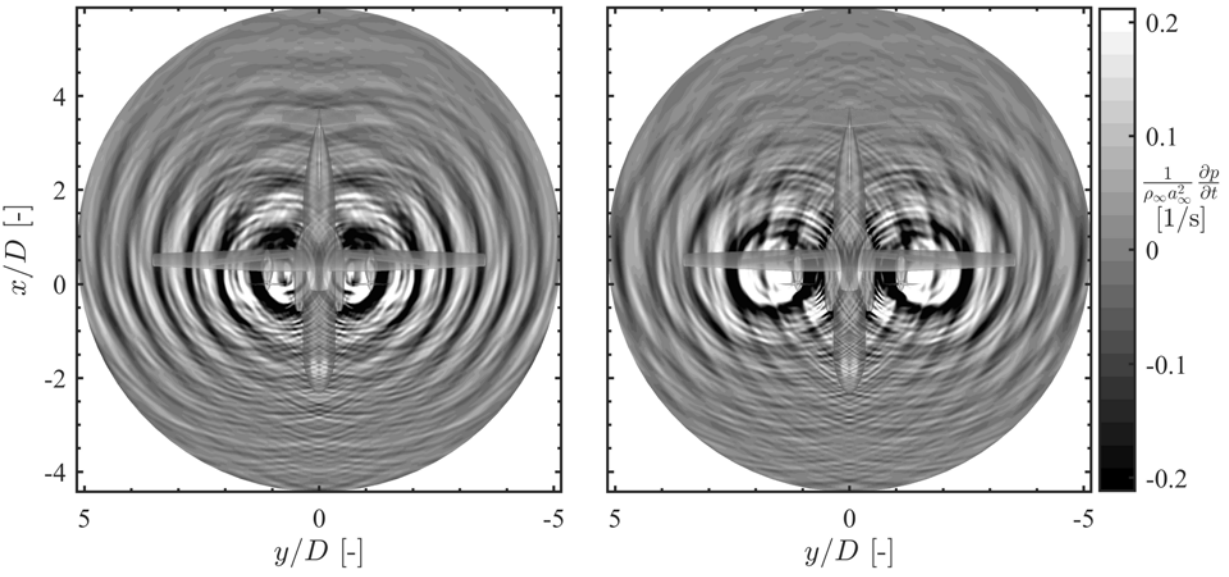

(a) *Outboard up* (b) *Inboard up*

Fig. 25 Dilatation field on a horizontal plane positioned approximately one propeller diameter below the aircraft centre. Data extracted from direct CFD results in the range $1/4 < f/BPF < 4$. Configuration with propeller rotating outboard up in (a) while rotating inboard up in (b).

differences, we report in Fig. 26 the SPL spectra at $\theta = -105°$, which is the microphone location where the SBW–CNT deviation is most pronounced. At this position, the SBW configuration exhibits an increase in broadband noise between the first two blade-passing harmonics. Since the strut was shown in Section V.C to have no measurable effect on the propeller loading, the observed broadband excess is attributed to the interaction between the propeller slipstream and the strut surface. Although this local increase is measurable, its magnitude remains small compared with the dominant sources, such as the propeller noise, the propeller–wing aerodynamic interaction, and the propeller–fuselage acoustic interaction. Consequently, it does not produce a noticeable change in the integrated OSPL or in the far-field noise footprint as we will see in the next section.

2. On ground noise

The analysis of installation effects on aircraft noise is concluded by investigating the Effective Perceived Noise Level (EPNL) footprint during take-off. EPNL is computed according to the FAR procedure [55], considering a trajectory that includes a 1.2 km take-off segment and a climbing phase with a rate of climb (RoC) of 7 m/s. The flight path is approximately 10 km long (from $x = 0$ to $x = -9750$ m), with a vertical altitude difference of 1 km (from $z = 100$ to $z = 1100$ m) and a total duration of 140 seconds. The free-stream conditions are presented in Section IV, and an atmospheric relative humidity of 70% is considered. It is important to note that this trajectory is not intended to capture variations in aircraft performance, but rather to serve as a fixed reference path for acoustic footprint evaluation.

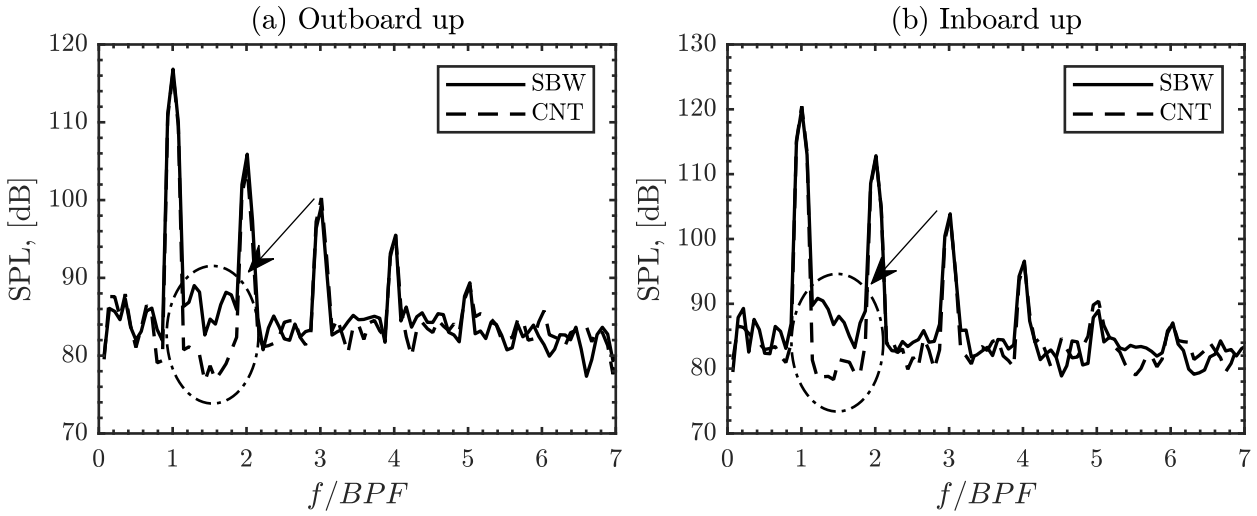

Fig. 26 SPL spectra computed at the microphone location at $\theta = -105°$ (y-plane). Comparison between cantilever (CNT) and strut-braced (SBW) for propeller rotating outboard up (a) and inboard up (b).

Accordingly, the noise hemisphere was generated from the CFD solution at a single flight condition, representative of the beginning of the climb segment.

Fig. 27 shows the EPNL on a plane 1.2 m above the ground over an area of 15×15 Km^2 for all aircraft configurations analyzed at both the rotation directions of the propeller. As expected, the EPNL shows that the highest noise levels occur at the beginning of the flight trajectory, i.e., when the distance between the noise source and the ground is the minimum. Then, for all cases, the on-the-ground noise levels gradually decrease along the flight direction as the noise source altitude increases. The noise on the ground is mainly radiated underneath the aircraft and in the upstream direction. In addition, compared to the inboard up configuration (Fig. 27, second row), higher noise levels are spread in the lateral direction by the outboard up configuration (Fig. 27, first row). This can be explained by the effect of the multi-body reflections discussed in the previous subsection concerning Fig. 20-(c).

For the certification procedure, it is necessary to look at the time history of the tone-corrected perceived noise levels, PNLT, at the flyover and lateral points. These are shown in Fig. 28. A summary of the most relevant values for the certification is also reported in Table 4. Overall, it can be observed that the noisiest configuration is the cantilever rotating inboard up, with around 100.8 and 100.9 EPNdB at the flyover and lateral point, respectively. At both certification points, the configuration produced noise levels more than 3 EPNdB higher than those of its respective isolated case and the installed configurations rotating in the opposite direction. Specifically, regarding the inboard up configuration, the SBW and CNT show similar results, with the SBW being half EPNdB quieter than the cantilever for both certification points. The isolated configuration reported 96.6 and 97 EPNdB at the flyover and lateral point, respectively. The differences between the installed and isolated configurations are mainly associated with an increase in the maximum PNLT, which occurs approximately when the aircraft flies over the points (vertical solid line in the figures). Indeed, the

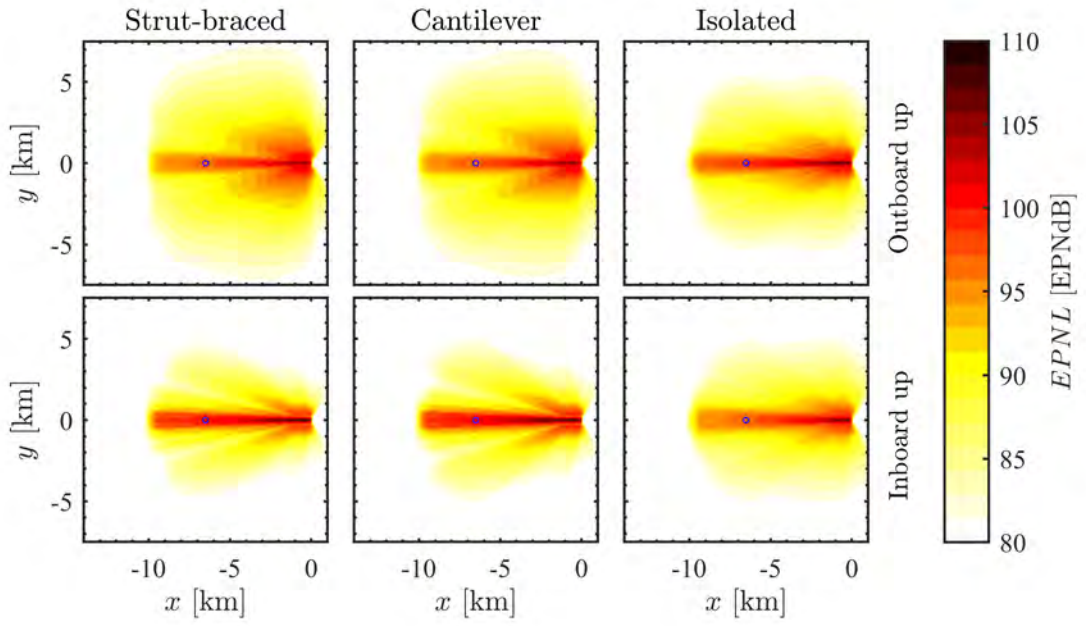

Fig. 27 Effective Perceived Noise Levels, $EPNL$, on ground for the different configurations analyzed. The blue circle represents the flyover certification point.

duration correction factor D is similar for all the cases. (between -1.5 and -2 EPNdB).

Looking at the outboard up configuration, an unexpected trend occurs since the EPNL of the isolated configuration is 2 EPNdB higher than the installed one in both certification points. Again, the differences are mainly due to a change in the maximum PNLT for all the cases except for the lateral point. At the lateral point, the SBW produced high noise levels for a longer time, resulting in a correction factor of almost zero. The differences between these values follow what is presented in the directivity section (Section V.F.1). Since the maximum PNLT is found when the aircraft passes over the certification points, we can infer that the related noise is due to sound radiation in the direction underneath the aircraft. Directivity plots shown in the previous section reported a reduction of the first BPF tone for the installed configurations rotating outboard up, and this was related to the presence of the fuselage sponson, which acts as an obstacle for sound waves coming from the propeller blades, preventing them from radiating under the aircraft. For the same reason, we see a reduction of EPNL at the certification points.

The same explanation can be used to justify the differences between the EPNL reported between the installed configurations rotating inboard up and the ones rotating outboard up.

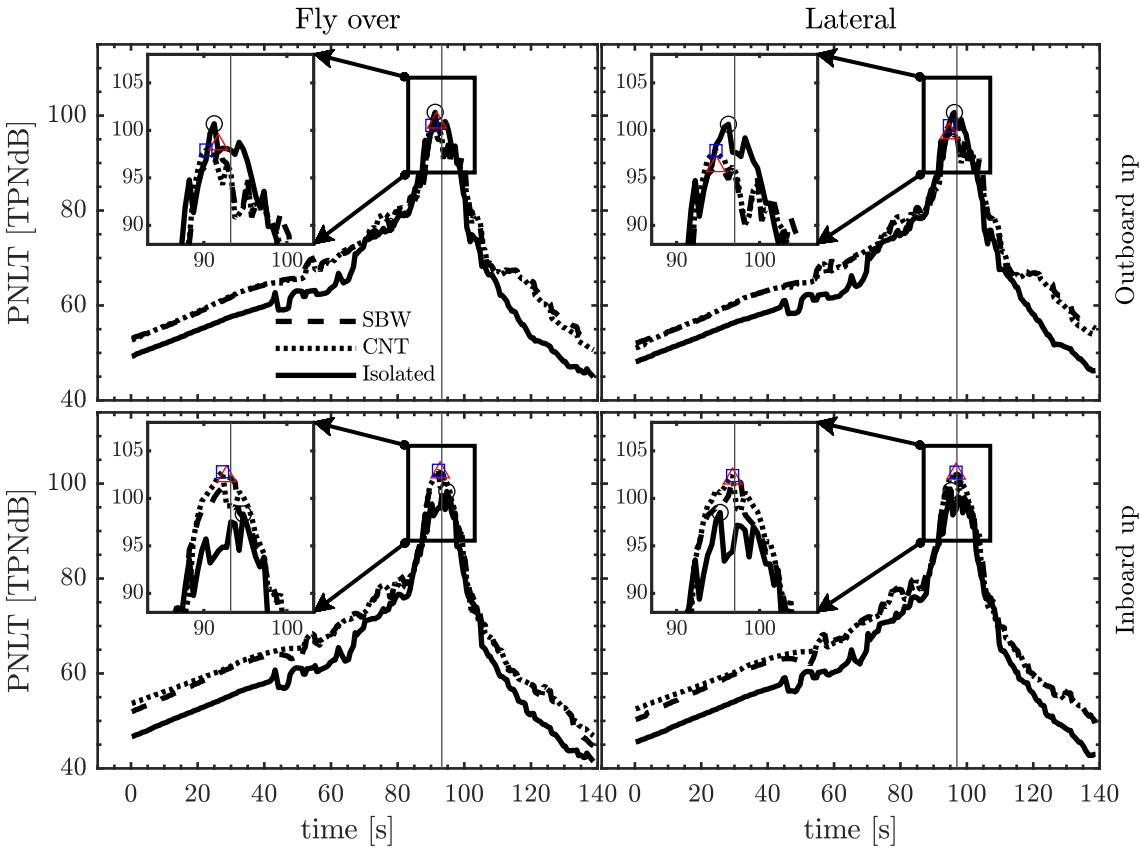

Fig. 28 Time history of Tone Corrected Perceived Noise Levels (PNLT) at the flyover point (first column) and lateral point (second column) for different cases analyzed. Specifically, the first row graphs refer to the configurations rotating outboard up, whereas the second row refers to the ones rotating inboard up. Maximum PNLT are indicated with colored markers (△: SBW, □: CNT, ○: Isolated). Finally, the vertical solid line indicates the time when the aircraft flies above the respective certification point.

Table 4 Flyover and lateral noise data in decibels.

	Flyover						**Lateral**					
	Inboard Up			Outboard Up			Inboard Up			Outboard Up		
	EPNL	PLNTM	D	EPNL	PNTLM	D	EPNL	PLNTM	D	EPNL	PNTLM	D
SBW	100.5	102.3	−1.9	96.5	98.5	−2.1	100.2	102.1	−1.9	96.1	96.2	−0.2
CNT	100.8	102.8	−2.0	96.5	97.9	−1.4	100.9	102.4	−1.5	96.6	97.9	−1.2
ISO	96.6	98.4	−1.8	98.5	100.7	−2.2	97.0	98.5	−1.5	98.7	100.6	−2.0

VI. Conclusion

The need to reduce flight emissions has led to the development of new aircraft configurations, with the strut-braced wing emerging as a promising candidate for short-term implementation. However, this configuration presents new aerodynamic challenges, particularly regarding the interaction between the propeller and the overall aircraft structure. To this end, the numerical investigation of aerodynamic installation effects between the propeller slipstream and a strut-braced wing has been performed by analyzing a regional-transport strut-braced aircraft, at a high angle of attack ($\alpha = 10°$), employing VLES-LBM flow solver and hybrid CAA method.

The present research has been focused on the installation effect on (i) the aircraft aerodynamic efficiency, (ii) the wing loading, (iii) the blade loading, (iv) the unsteady surface pressure field on the wing, and (v) the aircraft's noise emission.

The interaction between the propeller and the overall aircraft led to a reduction of the aerodynamic efficiency, with respect to the ideal propeller-off configuration, of around 7% for the configuration with propellers rotating inboard up and 8% for the one rotating outboard up.

The analysis of the effect of the propeller slipstream on the wing loading corroborated previous numerical and experimental results. However, the present 3-D numerical simulations provided new insights into the increase of wing drag due to the nacelle-wing vortex. Moreover, the installation effects of the propeller slipstream over the strut were found to be beneficial in terms of aerodynamic efficiency.

The presence of the wing amplified the increase in the loading on the blade when it moves from the pressure to the suction side and the decrease in the opposite direction. Hence, the effects of the wing on the propeller resulted in an increased difference in loading observed on the blade during the two phases of the revolution. In addition, an asymmetry in the loading temporal distribution was shown, leading to a higher contribution of the secondary BPF harmonics to the far-field noise emitted from the aircraft. The strut did not affect the blade loading due to its relatively small size and load compared to the main wing.

The impingement of the propeller wake on a downstream body led to high-pressure fluctuations, with distinct effects observed on the wing and strut. On the wing, the tip vortex interaction created elongated lobes in the chord-wise direction, whereas the trailing vorticity affected a broader inner region with shorter interaction times. Conversely, the distinction between tip and trailing vorticity effects on the strut was less pronounced, resulting in a more uniform region of pressure fluctuations with potentially more significant impact. In addition, the identified strut-wake interaction and the consequent fluctuating field could be influenced by the inclination of the slipstream, varying with the angle of attack.

A combination of far-field and near-field noise analyses revealed the importance of multi-body reflections. It was demonstrated that the strut has minor effects on far-field noise. However, the direction of rotation is of primary importance. In particular, the installed configuration equipped with the propeller rotating outboard up reported 4 EPNdB lower noise than the configuration with the propeller rotating inboard up at both flyover and lateral certification points.

This results from a different interaction between the propeller and the fuselage in the two cases analyzed. Specifically, for the outboard up rotation case, the interaction led to a shadow region of noise just underneath the aircraft and, therefore, to a lower noise computed in the certification procedure. Furthermore, higher pressure fluctuations were found on the aircraft fuselage of the configuration rotating outboard up. The results also indicated that the main acoustic features are governed by the propeller–wing interaction, whereas the contribution of the strut is of secondary importance. This conclusion is specific to aircraft geometries where the ratio between the strut and wing loading is relatively low. For configurations with higher strut loading or different geometric proportions, stronger strut-induced effects may arise.

In conclusion, this study provides insights into the complex aerodynamic and aeroacoustic interactions in strut-braced aircraft. The findings contribute to the understanding of propeller installation effects on aerodynamic performance, noise emissions, and certification considerations.

Appendix

A. Aerodynamic Optimization Framework

The strut-braced wing shape was defined using the *in-house* optimization framework *WiMOT* (Wing Multi-objective Optimization Tool) with the aim to minimize aerodynamic drag in cruise.

The optimization framework is based on a gradient-free algorithm and on low/mid-fidelity CFD methods. Specifically, the aerodynamic performances are computed by combining the span-wise lift distribution obtained using a Vortex Lattice Method [65] and the sectional drag force obtained using a compressible Viscous/Inviscid Interaction Method for multi-element airfoils [66] at several sections along the wing-span; the optimum is computed using a genetic algorithm. The employed tool can take into account the aerodynamic interaction between multiple lifting surfaces, laminar-to-turbulent transition, and shock waves eventually occurring in the region enclosed by the wing and the strut efficiently and reliably. Furthermore, the possibility of incurring local minima is minimized by using gradient-free methods.

The objective function flow chart is shown in Fig. 29. The input represents the current state of the design variables (i.e., the parametrized geometry). After a first step, needed to pass from the parametrized geometry to the actual one, Athena Vortex Lattice (AVL) [65] is used to compute the induced drag, C_{D_i}, and the lift distribution on the wing and the strut. These lift distributions are then used to compute 2-D drag coefficients, $C_{d_{v,w}}(y)$, at a certain number of sections y by means of MSES [66]. Finally, the total drag coefficient is obtained as:

$$J = C_{D_i} + \frac{2}{S}\int_0^{b/2} C_{d_{v,w}}(y)\, c(y)\, dy\,. \tag{8}$$

The framework is implemented in MATLAB and exploits its explicit multi-core parallel computing features to

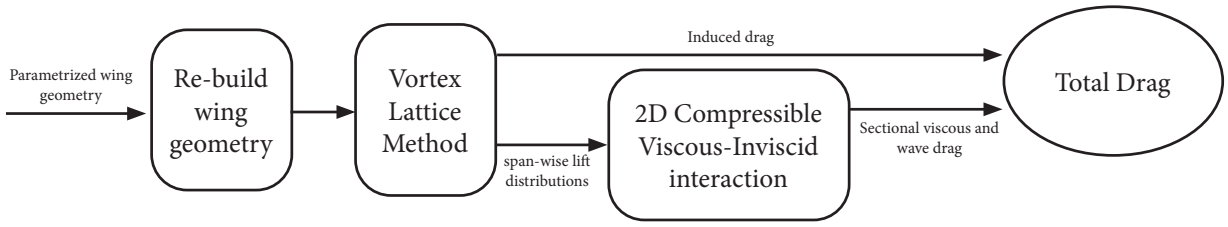

Fig. 29 *WiMOT* objective function flow chart.

analyze every element of the population simultaneously. To deal with multiple flight conditions, the algorithm uses the weighted-sum method [67]. The tool is meant for the optimization of up to two lifting surfaces (i.e., the wing and the strut), but can also be used for mono-wing systems or just single airfoils. The wing geometry is schematized as a combination of multiple span-wise sections. For each of these sections, the twist and swept angle, the chord size, and the airfoil shape can be included in the design vector. The airfoil shape is efficiently parametrized using the Class-Shape function Transformation (CST) [68]. Then, the airfoil shape is described by a set of $2n$ Bernstein polynomial coefficients, where n is the order selected for the Bernstein polynomials.

Eventually, linear equality and inequality constraints have been defined to ensure the regularity of the airfoils' shape. These constraints are directly translated to Bernstein's coefficients to enhance optimization speed. Specifically, by substituting Eq. (17) and (19) of Kulfan's paper [68], in the conditions (i) $z_u(x) > z_l(x) \forall x$, to avoid intersecting airfoils, and (ii) $\int_0^1 [z_u(x/c) - z_l(x/c)]\, d(x/c) = A_0$, to prescribe a fixed internal area A_0, the following constraints have been defined:

$$\sum_{i=1}^{n} (A_{u_i} - A_{l_i}) S_i(\psi) \geq -\psi \frac{\zeta_{TE_u} - \zeta_{TE_l}}{C_{N_2}^{N_1}(\psi)} \quad \forall \psi \in [0,1] \tag{9}$$

$$\sum_{i=1}^{n} (A_{u_i} - A_{l_i}) \binom{n}{i} \int_0^1 \psi^{N_1+i} (1-\psi)^{N_2+n-1} d\psi = A_0 - \frac{\zeta_{TE_u} - \zeta_{TE_l}}{2} \tag{10}$$

where n is the order of the Bernstein polynomial. A_u and A_l are the upper side and lower side Bernstein coefficients, respectively. $\psi = x/c$ is the non-dimensional x coordinate (along the airfoil chord). $\zeta = z/c$ is the non-dimensional z coordinate (normal to the airfoil chord). N_1 and N_2 are the parameters defining the class of the geometry shape, in this case equal to 0.5 a 1.0, respectively. S_i is the component shape function (defined in Eq. (12) in [68]). $C_{N_2}^{N_1}$ is the class function (defined in Eq. (15) in [68]). Eventually, the integrals in Eq. (10) are computed and stored before the optimization.

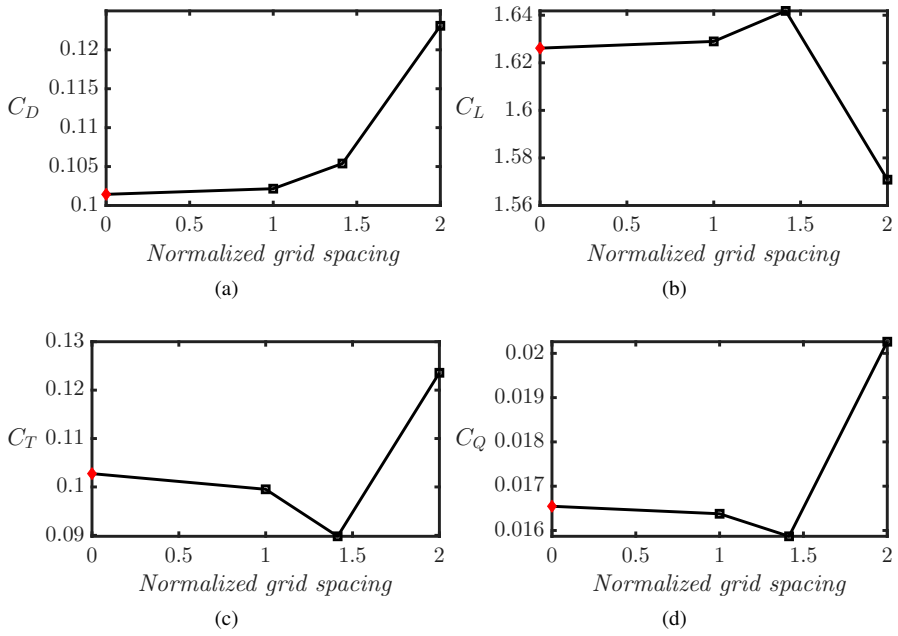

Fig. 30 Convergence plots showing the variation of aerodynamic coefficients C_D, C_L, C_T, and C_Q with normalized grid spacing. Each plot illustrates the effect of grid refinement on the respective coefficient. The red point represents the Richardson extrapolation, providing an estimate of the true solution by accounting for numerical error in the grid discretization.

B. Grid Convergence Analysis

This section presents a grid convergence analysis addressing both steady aerodynamic forces and unsteady far-field noise predictions.

In Fig.30, the variation of the time-averaged aerodynamic coefficient with the grid refinement is shown. The analysis was carried out considering the strut-braced installed configuration with the propeller rotating outboard up as the representative case. Analogous mesh topology and size were used for the other cases. In Fig. 30-(a) and (b), drag and lift coefficient exerted by the aircraft, excluding the contribution of the propeller, are presented and scaled using the following reference parameters: $q_{ref} = 1/2\rho_\infty V_\infty^2 = 2832.2\,Pa$ and $S_{ref} = 73.3\,m^2$. In Fig.30-(c) and (d), instead, propeller thrust and torque coefficients are shown and scaled by $q_{ref_{prop}} = \rho n^2 D^2 = 10476\,Pa$, $S_{ref_{prop}} = D^2 = 25.30\,m^2$ and $l_{ref_{prop}} = D$. Characteristics of the three meshes are reported in Table 5. Richardson extrapolation, shown in red in the figure, was computed to estimate the asymptotic solution for grid spacing going to zero. Based on this analysis, the *medium* grid was found to be the most efficient choice, balancing accuracy and computational cost and providing results reasonably close to the Richardson extrapolation.

To complement the aerodynamic analysis, the grid convergence of the far-field acoustic predictions was also assessed. The comparison between the *medium* and *fine* grid levels is reported in Fig. 31, which presents the Overall Sound Pressure Level (OASPL) directivity in three characteristic planes of the aircraft. The predicted directivity patterns

Table 5 Comparison of aerodynamic coefficients (C_L, C_D, C_T, C_Q) for different mesh resolutions. Each row represents a level of grid refinement (Coarse, Medium, Fine), with the corresponding normalized grid spacing $\frac{\Delta x}{\Delta x_{\text{fine}}}$, time step $\Delta t/T$, and number of voxels in millions. The Richardson extrapolation row provides an estimate of the value for each coefficient as grid spacing approaches zero.

	$\frac{\Delta x}{\Delta x_{fine}}$	$\Delta t/T$	Voxels (M)	C_L	C_D	C_T	C_Q
Coarse	2	2.8607e-04	168.60	1.570851	0.123086	0.123583	0.020263
Medium	$\sqrt{2}$	3.5759e-05	438.42	1.641828	0.105392	0.089805	0.015868
Fine	1	2.5261e-05	988.74	1.628995	0.102157	0.099513	0.016377
Extrapolation	0	0	∞	1.626163	0.101433	0.102750	0.016547

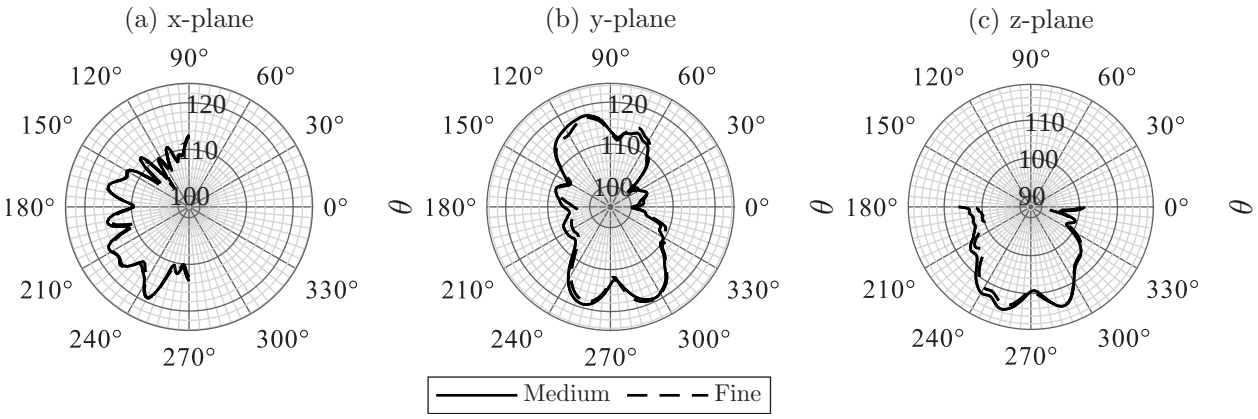

Fig. 31 OSPL directivity comparison in the aircraft's frontal plane (a), aircraft's symmetry plane (b) and aircraft horizontal plane (c). Comparison between medium and fine grid levels.

exhibit consistent features across the two grids, with average differences of approximately 0.5 dB, 0.9 dB, and 1.1 dB in the x-, y-, and z-planes, respectively. These differences are within the expected range of numerical uncertainty for broadband propeller noise simulations, indicating satisfactory convergence of the computed acoustic field.

In addition, Fig. 32 compares the SPL spectra obtained via the Ffowcs Williams–Hawkings (FWH) acoustic analogy at a reference microphone positioned 25 m below the aircraft on its symmetry plane. The two spectra show excellent agreement across the full frequency range, confirming that the medium grid accurately resolves the dominant tonal and broadband components of the radiated sound field. Accordingly, the medium grid resolution is employed for all subsequent aerodynamic and aeroacoustic analyses presented in this paper.

Finally, a note is made on the tip-vortex resolution. Accurately resolving and preserving rotor tip vortices is essential for capturing installation effects, yet achieving the 15-point core resolution suggested by Dacles-Mariani et al. [69] is generally impractical for full-scale cases. In the present LBM–VLES simulation, the roll-up occurs within VR13–15 and stabilizes in VR11 with a core diameter of about 10–18 cm (4–8 voxels per core). A finer-grid test produced slightly higher circulation but similar topology and trajectories, confirming that the main vortex evolution is well captured at the current resolution. Further refinement would likely improve the quantitative prediction of vortex circulation, but was not

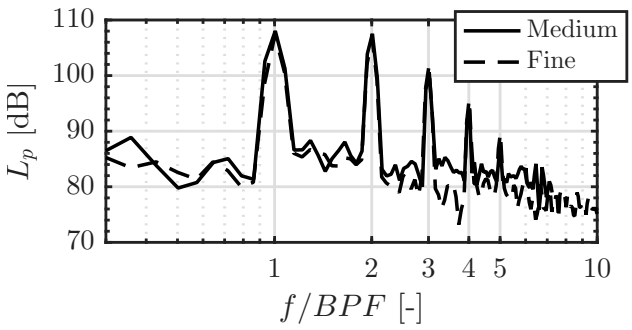

Fig. 32 Sound pressure level obtained through the application of FWH acoustics analogy. The microphone is located 25 m below the aircraft in its symmetry plane. Comparison between different grid resolutions.

computationally feasible within the scope of this work.

C. Comparison between FW-H permeable formulation and Direct Noise calculation

To validate far-field noise estimation, the hybrid CAA computation is herein compared with noise probes extracted directly from the CFD simulation. Again, the analysis was carried out considering the strut-braced installed configuration with the propeller rotating outboard up as the representative case. The microphones selected are the same used in Section V.F.1, shown respectively in Fig. 3. The CFD grid size and the sampling time at that location were defined to correctly capture propagating waves in the frequency range between 41.4 and 441.2 Hz (i.e., approximately 1/4 and 4 times the blade passing frequency). Therefore, for a fair comparison, both permeable and direct signals were filtered in that frequency range and then used to compute OSPL directivities shown in Fig. 33. Results show a reliable match within $1-2\,dB$ across all locations except for a few microphones positioned directly downstream of the aircraft (Figs. 33-(b) and (c) around $\theta = 0°$). At these locations, the BPF tonal contributions have been shown to be less important, and the mismatch is likely due to some interaction of the aircraft wake and the FW-H surface, which does not affect the conclusion drawn in Section V.F on the installation effects.

Acknowledgments

The authors gratefully acknowledge financial support from the Clean Aviation Joint Undertaking under the HERWINGT project (grant agreement No. 101102010). The granting authority receives support from the European Union's Horizon Europe research and innovation program and the Clean Aviation Joint Undertaking members other than the Union. Views and opinions expressed are, however, those of the author(s) only and do not necessarily reflect those of the European Union or Clean Aviation Joint Undertaking. Neither the European Union nor the granting authority can be held responsible for them. This work used the Dutch national e-infrastructure with the support of the SURF Cooperative using grant no. EINF-9416. The authors made use of an artificial intelligence–based language model (ChatGPT, OpenAI) for the refinement of grammar and language clarity.

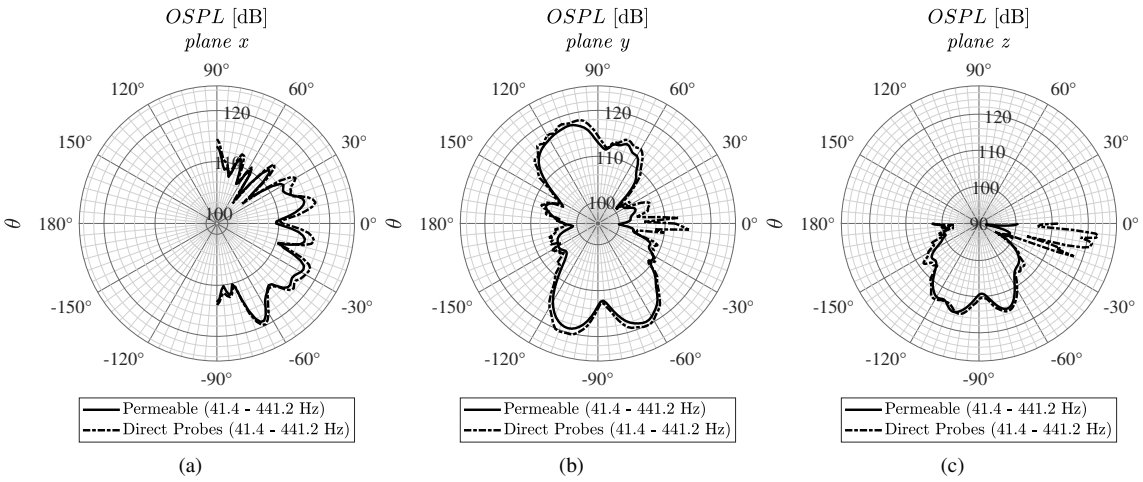

Fig. 33 Comparison of overall sound pressure level, OSPL, directivity between FW-H permeable acoustic analogy and direct noise measurement. Results are filtered in the frequency range in which direct probes have been sampled. Microphone locations relative to the permeable surface are shown in Fig. 3.

References

[1] Gur, O., Schetz, J. A., and Mason, W. H., "Aerodynamic Considerations in the Design of Truss-Braced-Wing Aircraft," *Journal of Aircraft*, Vol. 48, No. 3, 2011, pp. 919–939. https://doi.org/10.2514/1.C031171.

[2] Gundlach, J. F., Tetrault, P.-A., Gern, F. H., Nagshineh-Pour, A. H., Ko, A., Schetz, J. A., Mason, W. H., Kapania, R. K., Mason, W. H., Grossman, B., and Haftka, R. T., "Conceptual Design Studies of a Strut-Braced Wing Transonic Transport," *Journal of Aircraft*, Vol. 37, No. 6, 2000, pp. 976–983. https://doi.org/10.2514/2.2724, URL https://doi.org/10.2514/2.2724.

[3] Gern, F. H., Ko, A., Sulaeman, E., Gundlach, J. F., Kapania, R. K., and Haftka, R. T., "Multidisciplinary design optimization of a transonic commercial transport with strut-braced wing," *Journal of Aircraft*, Vol. 38, 2001, pp. 1006–1014. https://doi.org/10.2514/2.2887.

[4] Meadows, N. A., Schetz, J. A., Kapania, R. K., Bhatia, M., and Seber, G., "Multidisciplinary Design Optimization of Medium-Range Transonic Truss-Braced Wing Transport Aircraft," *Journal of Aircraft*, Vol. 49, No. 6, 2012, pp. 1844–1856. https://doi.org/10.2514/1.C031695.

[5] Chakraborty, I., Nam, T., Gross, J. R., Mavris, D. N., Schetz, J. A., and Kapania, R. K., "Comparative Assessment of Strut-Braced and Truss-Braced Wing Configurations Using Multidisciplinary Design Optimization," *Journal of Aircraft*, Vol. 52, No. 6, 2015, pp. 2009–2020. https://doi.org/10.2514/1.C033120.

[6] Moerland, E., Pfeiffer, T., Böhnke, D., Jepsen, J., Freund, S., Liersch, C. M., Chiozzotto, G. P., Klein, C., Scherer, J., Hasan, Y. J., and Flink, J., *On the Design of a Strut-Braced Wing Configuration in a Collaborative Design Environment*, 17th AIAA Aviation Technology, Integration, and Operations Conference, 2017. https://doi.org/10.2514/6.2017-4397.

[7] Secco, N. R., and Martins, J. R. R. A., "RANS-Based Aerodynamic Shape Optimization of a Strut-Braced Wing with Overset Meshes," *Journal of Aircraft*, Vol. 56, No. 1, 2019, pp. 217–227. https://doi.org/10.2514/1.C034934.

[8] Chau, T., and Zingg, D., "Fuel burn evaluation of a transonic strut-braced-wing regional aircraft through multipoint aerodynamic optimisation," *The Aeronautical Journal*, Vol. 127, No. 1308, 2023, p. 305–329. https://doi.org/10.1017/aer.2022.64.

[9] Droney, C. K., Sclafani, A. J., Harrison, N. A., Grasch, A. D., and Beyar, M. D., "Subsonic Ultra Green Aircraft Research: Phase III-Mach 0.75 Transonic Truss-Braced Wing Design," , 2020. URL https://ntrs.nasa.gov/api/citations/20205005698/downloads/NASACR20205005698_0208%20PUBLIC-rev2.pdf.

[10] Carrier, G., Atinault, O., Dequand, S., Hantrais-Gervois, J.-L., Liauzun, C., Paluch, B., A.-M., Rodde, Toussaint, C., and Onera, "Investigation of a Strut-Braced Wing Configuration for Future Commercial Transport," 2012. URL https://www.icas.org/ICAS_ARCHIVE/ICAS2012/PAPERS/597.PDF.

[11] Magionesi, F., Dubbioso, G., Muscari, R., and Di Mascio, A., "Modal analysis of the wake past a marine propeller," *Journal of Fluid Mechanics*, Vol. 855, 2018, p. 469–502. https://doi.org/10.1017/jfm.2018.631.

[12] Saunders, D. C., and Marshall, J. S., "Transient lift force on a blade during cutting of a vortex with non-zero axial flow," *Journal of Fluid Mechanics*, Vol. 819, 2017, p. 258–284. https://doi.org/10.1017/jfm.2017.188.

[13] Sinnige, T., de Vries, R., Corte, B. D., Avallone, F., Ragni, D., Eitelberg, G., and Veldhuis, L. L. M., "Unsteady Pylon Loading Caused by Propeller-Slipstream Impingement for Tip-Mounted Propellers," *Journal of Aircraft*, Vol. 55, No. 4, 2018, pp. 1605–1618. https://doi.org/10.2514/1.C034696.

[14] Veldhuis, L., "Review of propeller-wing aerodynamic interference. ICAS 2004-6.3.1," *24th International Congress of the Aeronautical Sciences, Yokohama, Japan*, 2004.

[15] McAlpine, A., and Kingan, M., "Far-Field Sound Radiation Due to an Installed Open Rotor," *International Journal of Aeroacoustics*, Vol. 11, No. 2, 2012, pp. 213–245. https://doi.org/10.1260/1475-472X.11.2.213, URL https://doi.org/10.1260/1475-472X.11.2.213.

[16] Chirico, G., Barakos, G. N., and Bown, N., "Propeller installation effects on turboprop aircraft acoustics," *Journal of Sound and Vibration*, Vol. 424, 2018, pp. 238–262. https://doi.org/10.1016/j.jsv.2018.03.003, URL https://www.sciencedirect.com/science/article/pii/S0022460X1830172X.

[17] Posa, A., Broglia, R., and Balaras, E., "The wake structure of a propeller operating upstream of a hydrofoil," *Journal of Fluid Mechanics*, Vol. 904, 2020, p. A12. https://doi.org/10.1017/jfm.2020.680.

[18] Wang, L., yu Guo, C., Xu, P., and Su, Y., "Analysis of the wake dynamics of a propeller operating before a rudder," *Ocean Engineering*, 2019. https://doi.org/10.1016/j.oceaneng.2019.106250.

[19] Rockwell, D., "Vortex-Body Interactions," *Annual Review of Fluid Mechanics*, Vol. 30, No. Volume 30, 1998, 1998, pp. 199–229. https://doi.org/10.1146/annurev.fluid.30.1.199.

[20] Coton, F., Marshall, J., Galbraith, R., and Green, R., "Helicopter tail rotor orthogonal blade vortex interaction," *Progress in Aerospace Sciences*, Vol. 40, No. 7, 2004, pp. 453–486. https://doi.org/10.1016/j.paerosci.2004.11.001.

[21] Krishnamoorthy, S., and Marshall, J. S., "Three-dimensional blade–vortex interaction in the strong vortex regime," *Physics of Fluids*, Vol. 10, No. 11, 1998, pp. 2828–2845. https://doi.org/10.1063/1.869805.

[22] Marshall, J., "Models of secondary vorticity evolution during normal vortex-cylinder interaction," *AIAA Journal*, Vol. 40, 2002, pp. 170–172. https://doi.org/10.2514/3.15010.

[23] Marshall, J. S., "Vortex cutting by a blade. I - General theory and a simple solution," *AIAA Journal*, Vol. 32, No. 6, 1994, pp. 1145–1150. https://doi.org/10.2514/3.12113.

[24] Liu, X., and Marshall, J. S., "Blade penetration into a vortex core with and without axial core flow," *Journal of Fluid Mechanics*, Vol. 519, 2004, p. 81–103. https://doi.org/10.1017/S0022112004001302.

[25] Marshall, J. S., and Krishnamoorthy, S., "On the instantaneous cutting of a columnar vortex with non-zero axial flow," *Journal of Fluid Mechanics*, Vol. 351, 1997, p. 41–74. https://doi.org/10.1017/S0022112097007064.

[26] Green, R. B., Doolan, C. J., and Cannon, R. M., "Measurements of the orthogonal blade–vortex interaction using a particle image velocimetry technique," *Experiments in Fluids*, Vol. 29, No. 4, 2000, pp. 369–379. https://doi.org/10.1007/s003489900096.

[27] Muscari, R., Dubbioso, G., and Di Mascio, A., "Analysis of the flow field around a rudder in the wake of a simplified marine propeller," *Journal of Fluid Mechanics*, Vol. 814, 2017, p. 547–569. https://doi.org/10.1017/jfm.2017.43.

[28] Magionesi, F., Dubbioso, G., and Muscari, R., "Contribution of tip and hub vortex to the structural response of a marine rudder in the propeller slipstream," *Journal of Fluid Mechanics*, Vol. 946, 2022, p. A23. https://doi.org/10.1017/jfm.2022.558.

[29] Felli, M., and Falchi, M., "Propeller tip and hub vortex dynamics in the interaction with a rudder," *Experiments in Fluids*, Vol. 51, No. 5, 2011, pp. 1385–1402. https://doi.org/10.1007/s00348-011-1162-7.

[30] Felli, M., "Underlying mechanisms of propeller wake interaction with a wing," *Journal of Fluid Mechanics*, Vol. 908, 2021, p. A10. https://doi.org/10.1017/jfm.2020.792.

[31] Teruna, C., Rego, L., Casalino, D., Avallone, F., and Ragni, D., "A Numerical Study on Aircraft Noise Mitigation Using Porous Stator Concepts," *Aerospace*, Vol. 9, No. 70, 2022. https://doi.org/10.3390/aerospace9020070.

[32] Romani, G., Ye, Q., Avallone, F., Ragni, D., and Casalino, D., "Numerical analysis of fan noise for the NOVA boundary-layer ingestion configuration," *Aerospace Science and Technology*, Vol. 96, 2020, p. 105532. https://doi.org/10.1016/j.ast.2019.105532.

[33] Casalino, D., van der Velden, W. C., and Romani, G., "Community Noise of Urban Air Transportation Vehicles," *AIAA Scitech 2019 Forum*, 2019. https://doi.org/10.2514/6.2019-1834, URL https://arc.aiaa.org/doi/abs/10.2514/6.2019-1834.

[34] Avallone, F., Casalino, D., and Ragni, D., "Impingement of a Propeller Slipstream on a Leading Edge with a Flow-Permeable Insert: A Computational Aeroacoustic Study," *International Journal of Aeroacoustics*, Vol. 17, No. 6-8, 2018. https://doi.org/10.1177/1475472x18788961.

[35] Romani, G., and Casalino, D., "Rotorcraft Blade-Vortex Interaction Noise Prediction using the Lattice-Boltzmann Method," *Aerospace Science and Technology*, Vol. 800, 2019, pp. 147–157. https://doi.org/10.1016/j.ast.2019.03.029.

[36] Lockard, D., Humphreys, W., Khorrami, M., Fares, E., Casalino, D., and Ravetta, P., "Comparison of Computational and Experimental Microphone Array Results for an 18%-Scale Aircraft Model," *International Journal of Aeroacoustics*, Vol. 16, No. 4-5, 2017, pp. 358–381. https://doi.org/10.1177/1475472x17718724.

[37] Hazir, A., and Casalino, D., "Lattice Boltzmann Based Aeroacoustic Simulation of Turbofan Noise Installation Effects," *Proceedings of the 23rd International Congress on Sound and Vibration, Athens, Greece*, 2016.

[38] Fares, E., Casalino, D., and Khorrami, M. R., "Evaluation of Airframe Noise Reduction Concepts via Simulations Using a Lattice Boltzmann Approach," 2015. https://doi.org/10.2514/6.2015-2988, URL https://arc.aiaa.org/doi/abs/10.2514/6.2015-2988.

[39] Khorrami, M. R., Fares, E., and Casalino, D., "Towards Full Aircraft Airframe Noise Prediction: Lattice Boltzmann Simulations," 2014. https://doi.org/10.2514/6.2014-2481, URL https://arc.aiaa.org/doi/abs/10.2514/6.2014-2481.

[40] Cerizza, D., Casalino, D., and Gonzalez-Martino, I., "An Extension of the Acoustics Evaluation of the NASA SDT turbofan with Lattice-Boltzmann methods," 2022. https://doi.org/10.2514/6.2022-2886, URL https://arc.aiaa.org/doi/abs/10.2514/6.2022-2886.

[41] Casalino, D., Avallone, F., Gonzalez-Martino, I., and Ragni, D., "Aeroacoustic Study of a Wavy Stator Leading Edge in a Realistic Fan/OGV Stage," *Journal of Sound and Vibration*, Vol. 442, 2019, pp. 138–154. https://doi.org/10.1016/j.jsv.2018.10.057.

[42] Gonzalez-Martino, I., and Casalino, D., "Fan Tonal and Broadband Noise Simulations at Transonic Operating Conditions Using Lattice-Boltzmann Methods," 2018. https://doi.org/10.2514/6.2018-3919, URL https://arc.aiaa.org/doi/abs/10.2514/6.2018-3919.

[43] Casalino, D., Hazir, A., and Mann, A., "Turbofan Broadband Noise Prediction using the Lattice Boltzmann Method," *AIAA Journal*, Vol. 56, No. 2, 2017. https://doi.org/10.2514/1.J055674.

[44] Gopalakrishnan, P., Chen, H., Zhang, R., Jammalamadaka, A., and Li, Y., "Lattice Boltzmann Solver Enforcing Total Energy Conservation," , Jun 2022. URL https://patents.google.com/patent/US12079552B2/en, [Online; accessed 19-Nov-2025].

[45] Chen, H., Zhang, R., and Gopalakrishnan, P., "Lattice Boltzmann Collision Operators Enforcing Isotropy and Galilean Invariance," , Dec 2015. URL https://patents.google.com/patent/US20150356217A1/en, [Online; accessed 19-Nov-2025].

[46] Yakhot, V., and Orszag, S. A., "Renormalization group analysis of turbulence. I. Basic theory," *Journal of Scientific Computing*, Vol. 1, No. 1, 1986, p. 3–51. https://doi.org/10.1007/bf01061452, URL https://doi.org/10.1007/bf01061452.

[47] Chen, H., Kandasamy, S., Orszag, S., Shock, R., Succi, S., and Yakhot, V., "Extended Boltzmann Kinetic Equation for Turbulent Flows," *Science*, Vol. 301, No. 5633, 2003, pp. 633–636. https://doi.org/10.1126/science.1085048.

[48] Chen, H., Orszag, S. A., Staroselsky, I., and Succi, S., "Expanded analogy between Boltzmann kinetic theory of fluids and turbulence," *Journal of Fluid Mechanics*, Vol. 519, 2004, p. 301–314. https://doi.org/10.1017/S0022112004001211.

[49] Teixeira, C., "Incorporating Turbulence Models into the Lattice-Boltzmann Method," *International Journal of Modern Physics C*, Vol. 09, 1998, pp. 1159–1175. https://doi.org/10.1142/s0129183198001060.

[50] Shao, W., and Li, J., "Review of Lattice Boltzmann Method Applied to Computational Aeroacoustics," *Archives of Acoustics*, Vol. vol. 44, No. No 2, 2019, pp. 215–238. https://doi.org/10.24425/aoa.2019.128486.

[51] Ffowcs Williams, J. E., and Hawkings, D. L., "Sound generation by turbulence and surfaces in arbitrary motion," *Philosophical Transactions of the Royal Society of London. Series A, Mathematical and Physical Sciences*, Vol. 264, No. 1151, 1969, pp. 321–342. https://doi.org/10.1098/rsta.1969.0031.

[52] Lockard, D. P., "An Efficient, Two-Dimensional Implementation of the Ffowcs Williams and Hawkings Equation," *Journal of Sound and Vibration*, Vol. 229, No. 4, 2000, pp. 897–911. https://doi.org/https://doi.org/10.1006/jsvi.1999.2522.

[53] van der Velden, W., Casalino, D., Gopalakrishnan, P., Jammalamadaka, A., Li, Y., Zhang, R., and Chen, H., "Validation of Jet Noise Simulations and Resulting Insights of Acoustic Near Field," *AIAA Journal*, Vol. 57, 2019, pp. 1–12. https://doi.org/10.2514/1.J057970.

[54] Welch, P., "The use of fast Fourier transform for the estimation of power spectra: A method based on time averaging over short, modified periodograms," *IEEE Transactions on Audio and Electroacoustics*, Vol. 15, No. 2, 1967, pp. 70–73. https://doi.org/10.1109/TAU.1967.1161901.

[55] Archives, N., and Administration, R., "Title 14: Aeronautics and Space," , 2025. URL https://www.ecfr.gov/current/title-14, accessed: 2025-02-24.

[56] Casalino, D., Noelting, S., Fares, E., de Ven, T. V., Perot, F., and Bres, G., *Towards Numerical Aircraft Noise Certification: Analysis of a Full-Scale Landing Gear in Fly-Over Configuration*, 18th AIAA/CEAS Aeroacoustics Conference (33rd AIAA Aeroacoustics Conference), 2012. https://doi.org/10.2514/6.2012-2235, URL https://arc.aiaa.org/doi/abs/10.2514/6.2012-2235.

[57] Tétrault, P.-A., "Numerical Prediction of the Interference Drag of a Streamlined Strut Intersecting a Surface in Transonic Flow," Ph.D. thesis, Virginia Polytechnic Institute & State University, 2000.

[58] Mendez, S., Shoeybi, M., Lele, S. K., and Moin, P., "On the Use of the Ffowcs Williams-Hawkings Equation to Predict Far-Field Jet Noise from Large-Eddy Simulations," *International Journal of Aeroacoustics*, Vol. 12, No. 1-2, 2013, pp. 1–20. https://doi.org/10.1260/1475-472X.12.1-2.1.

[59] Spalart, P. R., Belyaev, K. V., Shur, M. L., Strelets, M. K., and Travin, A. K., "On the differences in noise predictions based on solid and permeable surface Ffowcs Williams–Hawkings integral solutions," *International Journal of Aeroacoustics*, Vol. 18, No. 6-7, 2019, pp. 621–646. https://doi.org/10.1177/1475472X19878934.

[60] Veldhuis, L., "Propeller Wing Aerodynamic Interference," Ph.D. thesis, Delft University of Technology, Delft, Netherlands, June 2005.

[61] Nederlof, R., Kooij, R., Veldhuis, L. L., and Sinnige, T., "Contribution of Swirl Recovery to the Induced Drag of a Propeller-Wing System – A Parametric Study," *AIAA AVIATION 2023 Forum*, 2023. https://doi.org/10.2514/6.2023-3543, URL https://arc.aiaa.org/doi/abs/10.2514/6.2023-3543.

[62] Duivenvoorden, R., Suard, N., Sinnige, T., and Veldhuis, L. L., *Experimental Investigation of Aerodynamic Interactions of a Wing with Deployed Fowler Flap under Influence of a Propeller Slipstream*, AIAA AVIATION 2022 Forum, 2022. https://doi.org/10.2514/6.2022-3216, URL https://arc.aiaa.org/doi/abs/10.2514/6.2022-3216.

[63] Hanson, D. B., "Sound from a propeller at angle of attack: a new theoretical viewpoint," *Proceedings of the Royal Society of London. Series A: Mathematical and Physical Sciences*, Vol. 449, No. 1936, 1995, pp. 315–328. https://doi.org/10.1098/rspa.1995.0046, URL https://royalsocietypublishing.org/doi/abs/10.1098/rspa.1995.0046.

[64] Goyal, J., Sinnige, T., Ferreira, C., and Avallone, F., "Effect of Angle of Attack on Propeller Aeroacoustics at Positive and Negative Thrust," *Journal of Aircraft*, 2025. https://doi.org/10.2514/1.C038073.

[65] Drela, M. and Youngren, H., "Athena Vortex Lattice," http://web.mit.edu/drela/Public/web/avl/, Accessed: 2023-12-01, 2023.

[66] Drela, M., "MSES - Software for High-Lift Multi-element Airfoil Configuration," http://web.mit.edu/drela/Public/web/mses/, Accessed: 2023-12-01, 2023.

[67] Martins, J. R. R. A., and Ning, A., *Engineering Design Optimization*, Cambridge University Press, Cambridge, UK, 2022. https://doi.org/10.1017/9781108980647, URL https://mdobook.github.io.

[68] Kulfan, B. M., "Universal Parametric Geometry Representation Method," *Journal of Aircraft*, Vol. 45, No. 1, 2008, pp. 142–158. https://doi.org/10.2514/1.29958.

[69] Dacles-Mariani, J., Zilliac, G. G., Chow, J. S., and Bradshaw, P., "Numerical/experimental study of a wingtip vortex in the near field," *AIAA Journal*, Vol. 33, No. 9, 1995, pp. 1561–1568. https://doi.org/10.2514/3.12826, URL https://arc.aiaa.org/doi/10.2514/3.12826.